CHAPTER 6

Charge Density Wave Current Oscillations and Interference Effects

S.E. BROWN

Los Alamos National Laboratory
Los Alamos, New Mexico 87545, USA

and

A. ZETTL

Department of Physics
University of California at Berkeley
Berkeley, California 94720, USA

Charge Density Waves in Solids
Edited by
L.P. Gor'kov and G. Grüner

Contents

1. Introduction 225
2. Models of CDW motion and oscillation phenomena 229
   2.1. Single degree of freedom models 229
   2.2. Classical models with many degrees of freedom 231
   2.3. Current oscillations and microscopic pinning 233
   2.4. The tunneling model and current oscillations 235
   2.5. Phase-slip processes 237
3. Experimental issues pertaining to the narrow-band noise 238
   3.1. Volume dependence of the oscillations 238
   3.2. Periodicity of the potential 242
   3.3. Statistical measurement of the narrow-band noise 245
4. Electronic interference effects 246
   4.1. Shapiro steps 247
   4.2. Single degree of freedom models for the interference 254
   4.3. Internal modes and relevant time scales 257
   4.4. Many degree of freedom models for the interference 262
5. Driven CDWs and the theory of nonlinear dynamics 266
   5.1. Competing periodicities: the circle map 266
   5.2. CDW switching and transitions to chaos 269
      5.2.1. Mode locking and chaos 270
      5.2.2. Models for the switching and chaotic response 272
6. Relevant length scales and domain structure 278
   6.1. Intrinsic phase and velocity domains 278
   6.2. Temperature gradient effects 281
7. Electro-elastic interference 284
   7.1. Elastic mode locking 284
   7.2. Models for the elastic mode locking 285
8. Conclusion 288

References 289

1. *Introduction*

One of the more interesting and controversial discoveries associated with transport by charge-density waves (CDWs) was the observation of distinct oscillations in the linear-chain compound $NbSe_3$ (Fleming and Grimes 1979). The oscillations have become known as narrow-band noise (NBN) because of the fluctuating character of the response and to contrast it with a broad-band component that also characterizes CDW response. Rich harmonic content is typical for the oscillatory behavior and is illustrated in the spectral analysis of fig. 1.1 (taken from the original paper by Fleming and Grimes). Also seen is the $1/f$-like behavior at lower frequencies that became known as broad-band noise (BBN). The current oscillations appear only above a sharp threshold electric field E_T that also signifies the onset of the non-Ohmic conductivity. As the dc field is increased, the fundamental frequency increases monotonically from zero. CDW conduction noise can be similarly observed if a constant total current is applied to the crystal and the response voltage is monitored. This is in fact the more usual experimental situation for ease of detection and was the method used to generate the traces of fig. 1.1.

Conduction noise, either in the form of the oscillations or the broad-band noise, has become an accepted signature of collective dc transport in density-wave systems. Other CDW materials displaying the oscillations include TaS_3 in two forms (monoclinic and orthorhombic), $(TaSe_4)_2I$ and related materials, and the blue bronzes $K_{0.3}MoO_3$ and $Rb_{0.3}MoO_3$.

To illustrate why the oscillations are significant for these systems, we begin with a brief description of Fröhlich superconductivity. It was proposed by Fröhlich (1954) that superconductivity could result from the Peierls semiconducting (CDW) state in a one-dimensional metal by moving the distortion. In a system where the CDW and the lattice are commensurate, it costs energy to translate the distortion (often referred to as commensurability pinning), whereas the incommensurate CDW has no preferred position. Therefore, the CDW can move freely provided that it is incommensurate. The energy gap at the Fermi level prevents any damping from taking place by scattering of single electrons.

While all of the materials referred to above have incommensurate CDWs,

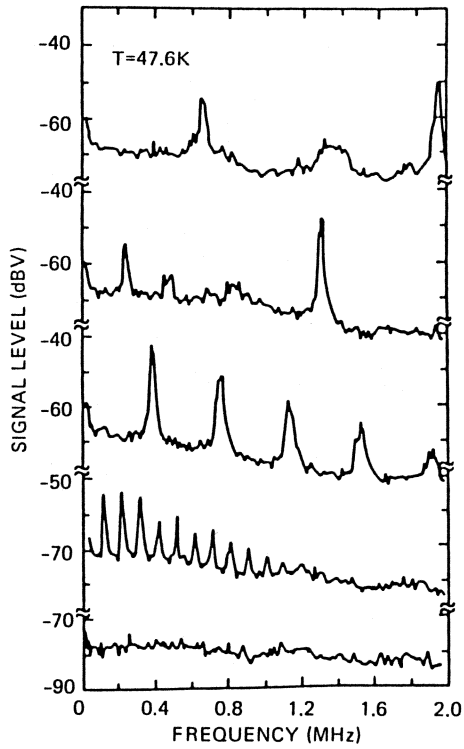

Fig. 1.1. Spectrum analysis of the voltage response for a series of current levels. (Fleming et al. 1979).

Fröhlich superconductivity is not observed for a variety of reasons. In real systems, the translational symmetry will be broken by impurities and other crystal defects, and presumably also by thermal phonons. These defects act to pin the phase of the charge-density wave, and to some degree must be responsible for a finite phase–phase coherence length. If the impurity concentration in the real CDW crystal is sufficiently small then the total pinning force may be quite weak, allowing for depinning by a modest dc electric field E_{dc} exceeding the depinning threshold E_T. In addition to allowing for the development of a pinning force, the low-energy phase distortions provide a possible mechanism for the dissipation of energy from the CDW. Pinning and damping are always observed experimentally.

Following the discovery of the narrow-band noise, it was conjectured that the velocity of the periodic charge-density wave was modulated because of the potential created by the pinning centers (Monceau et al. 1982, Grüner et al. 1981). The time-varying velocity was responsible for the measured oscillations. Associated with this intuitive interpretation is the postulate that

sliding CDW conduction and current oscillations are inseparable. In support is the observation that the excess (CDW) current and the fundamental frequency of the current oscillations are proportional. The relation is well established in $NbSe_3$ (Monceau et al. 1982, Zettl and Grüner 1984), TaS_3 (Brown and Grüner 1985), and $K_{0.3}MoO_3$. Figure 1.2 is an example depicting the linearity from Zettl and Grüner (1984).

It is often convenient to draw analogies to systems exhibiting similar behavior to CDWs, summarized by a dc threshold field for nonlinear conduction and oscillation phenomena above that threshold. Superconducting tunnel junctions and the damped, driven pendulum both share these properties. A finite current can flow at zero voltage in the junctions up to a critical density J_c. Above J_c, the dc voltage is a monotonically increasing function of the current; small voltage oscillations in addition to the dc are the ac Josephson effect. The frequency of the oscillations is linearly proportional to the dc voltage.

Measurements of the dc current–voltage (I–V) curves of the junctions when microwaves are applied is fundamentally important because constant voltage steps can be observed (Shapiro 1963) whenever the condition

$$n\hbar\omega_{app} = 2eV \tag{1.1}$$

is met, giving to a high precision the ratio $\hbar/e$. In eq. (1.1), V is the dc voltage across the junction, ω_{app} is the applied microwave frequency, and n is an integer. The name Shapiro step is often associated with this interference effect.

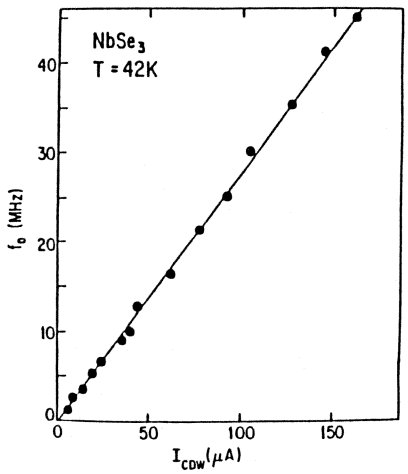

Fig. 1.2. Fundamental frequency of the oscillation response versus dc current level. (From Zettl and Grüner 1984).

The linear relationship between excess current and frequency of the oscillations for CDWs suggests that similar behavior may be realized for this system. First observed by Monceau et al. (1983), fig. 1.3 is a recording of differential resistance $\delta V/\delta I$ versus V for $NbSe_3$ from their paper. A peak in the differential resistance that increases to the Ohmic value below the threshold would indicate that the excess current does not change over the span in voltage where $\delta V/\delta I$ is high. The circumstances for which complete locking ($\delta V/\delta I$ = Ohmic value) occurs will be described in more detail in section 4. Complete locking can often be observed at harmonic steps, which correspond to the situation

$$p\omega_{app} = \omega_0, \tag{1.2}$$

where ω_0 is the fundamental angular frequency of the oscillations and p is an integer. Experimentally, ω_0 is determined by measuring the excess current and converting that to the equivalent fundamental frequency.

In addition to the harmonic steps, there has been considerable interest in the subharmonic steps, which satisfy $(p/q)\omega_{app} = \omega_0$. This is because of general interest in nonlinear driven systems, as well as being significant for the physics pertaining to sliding CDWs. These aspects will be described in sections 4 and 5. Results of mode-locking experiments in the presence of a temperature gradient in the context of velocity domain formation will be reviewed in section 6.

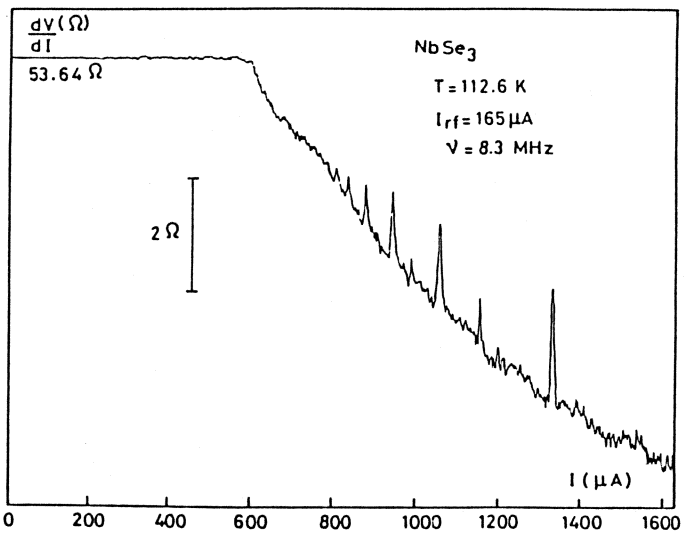

Fig. 1.3. Differential resistance versus dc current in the presence of a large radiofrequency ($\nu = 8.3$ MHz) drive. The peaks in the trace are the interference effects (from Monceau et al. 1982).

Physical properties of materials not directly associated with electronic transport can also be dramatically altered by sliding CDWs. The Young's modulus actually softens in several materials when the threshold field is exceeded. The application of an ac field complicates the situation still further, as steps are observed in the Young's modulus that correspond to the steps in the $I-V$ curve itself. The experiments and interpretation will be reviewed in section 7.

2. Models of CDW motion and oscillation phenomena

The reason for the current oscillations remains a controversial issue in the field of charge-density waves. Because the models that attempt to explain the conduction noise and interference effects appear elsewhere in this book, we give only a brief description as a way of introduction for the experiments.

2.1. Single degree of freedom models

The simplest model which includes most of the basic features of CDW conduction is a particle sitting in a washboard potential (Grüner et al. 1981, Monceau et al. 1980). An important neglection are the CDW internal degrees of freedom; for the moment we consider the CDW as a large, but finite sized, rigid object. It is pinned by anything that disrupts the translational invariance of the system (in the limit that the rigid CDW becomes infinite in extent, the total pinning force approaches zero). The electric field couples to the effective charge density ρ_0, defined by the spatially varying charge density $\rho(x)$

$$\rho(x) = \rho_0 + \rho_1 \cos[2k_F x + \phi(x)], \tag{2.1}$$

with k_F the Fermi wavevector, $\phi(x)$ the location of the CDW relative to the lab frame, and ρ_1 the amplitude of the charge modulation. The one-dimensional (1D) equation of motion can be written

$$m^* \frac{d^2x}{dt^2} + \Gamma \frac{dx}{dt} + \frac{dV}{dx} = eE(t), \tag{2.2}$$

where m^* is the effective mass of the CDW and Γ is a phenomenological damping constant. It is expected that m^* is much larger than the electron mass because the lattice distortion must move with the CDW. The simplest periodic potential is the cosine (also appropriate for the Josephson junction), for which eq. (2.2) becomes

$$m^* \frac{d^2x}{dt^2} + \Gamma \frac{dx}{dt} - 2k_F V_0 \sin(2k_F x) = eE(t). \tag{2.3}$$

Equation (2.3) contains many of the important features of CDW response: a finite threshold field $E_T = 2k_F V_0/e$, strong frequency-dependent conductivity, and a modulated drift velocity v_d under constant applied electric field. The CDW current density is given by

$$j_{CDW} = n_{CDW} e \bar{v}_d = n_{CDW} e \lambda f_0, \tag{2.4}$$

where n_{CDW} is the condensate density, $\bar{v}_d$ is the time-average velocity, λ is the CDW wavelength and f_0 is the fundamental frequency of the response oscillations. On a per chain basis, eq. (2.4) gives

$$j_c/f_0 = 2e \tag{2.5}$$

at $T = 0$. j_c is the CDW current carried on each chain, $\lambda = 2\pi/2k_F$ and the condensate density is $2k_F/\pi$ for one chain.

Failures of the single-particle model prompted more sophisticated treatment. With respect to the current oscillations and behavior around threshold there are several obvious problems. First, the ratio of the amplitude of the voltage oscillations δV to the threshold voltage V_T is far too small. Because it is the strength of the pinning leading to both effects, it is expected that $\delta V/V_T$ is on the order of unity. For example, in the high-field overdamped limit, the time-dependent velocity dx/dt is given by

$$\begin{aligned} \frac{dx}{dt} &= (e/\Gamma)(E - E_T \sin(2k_F x)) \\ &= (eE/\Gamma)(1 - (E_T/E)\sin(2k_F x)), \end{aligned} \tag{2.6}$$

with E the dc driving field. It follows that the oscillating current density $\delta j \sim \sigma_b E_T$ and therefore $\delta V \sim V_T$ (where σ_b is the high field conductivity of the CDW). Experimentally $NbSe_3$ shows the strongest current oscillation phenomena and smallest threshold field but still $\delta V/V_T \sim O(10^{-3})$ (Grüner and Zettl 1985). This can be explained by assuming that the pinning force somehow becomes reduced when the CDW is moving. However, it is important to note that this hypothesis requires giving up the main assumption that the CDW is rigid. Another feature of the single-particle model is the very different behavior produced when driven by a voltage or current. Graphed in fig. 2.1 are the two cases. A conductance from normal electrons is the reason for the current carried below threshold. However, the experiments never show any change as the source impedance is varied. Furthermore, the shape of the I–V curve is always concave up rather than down. Although it is possible that the curvature changes in the limit of high fields, that has never been observed.

The overdamped sinusoidal washboard model does not result in any subharmonic steps whatsoever. Attempts to explain them rely either on hypothesizing an effective potential with rich harmonic content or invoking

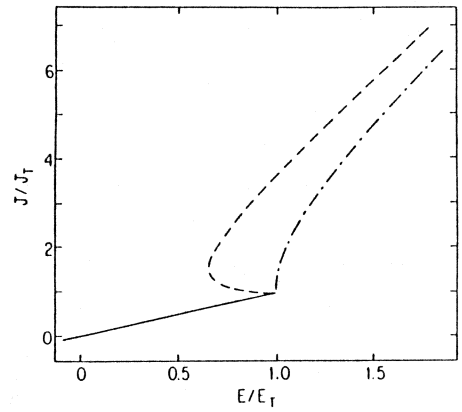

Fig. 2.1. Current–voltage (I–V) curve for the single-particle model. The presence of a channel for normal electrons accounts for the conductivity below the threshold field E_T. Note that the current drive (dashed curve) is double-valued with respect to the field. The dash-dotted curve denotes voltage drive.

a model that includes phase degrees of freedom. Because some unique aspects of the interference effects (section 4) share features with models that contain many effective degrees of freedom, we proceed to describe this modification of the classical transport model.

2.2. Classical models with many degrees of freedom

Near threshold, it is expected that impurity pinning of the phase will have very strong distortive effects on the CDW, so the easiest situation to handle is in the high-velocity limit, when the pinning centers can be treated perturbatively. Sneddon, Cross and Fisher (1982) (SCF) demonstrated that for this case the high field velocity takes the form:

$$j_c = \sigma_b E - c\sqrt{E}. \tag{2.7}$$

It was assumed that only long-wavelength distortions of the phase are important and therefore macroscopic equations are still appropriate. Adding an elasticity term to the equation of motion allows the CDW to distort as it moves over the impurities. That energy can be dissipated to other degrees of freedom in the crystal. It is important to note that the concave up form for the differential conductance is qualitatively consistent with the data.

Another significant feature that emerged from this treatment was that the velocity of the CDW was not modulated in time, so perhaps the observations are attributable to finite size effects. The argument in support of finite size can be put in simple terms by considering correlations of the

CDW between different regions. At zero velocity, the phase will be distorted by the impurities. The approximate distance over which the phase is nearly constant is the phase–phase correlation length $\langle\phi(0)\phi(x)\rangle$. Equivalently, a moving CDW described by a deformable model must have a finite velocity–velocity correlation length. Time-dependent velocities from different regions will have a random relative phase. The resulting sum over all the regions as the number of regions grows infinitely large has zero velocity modulation amplitude.

Fisher (1985) extended the work of SCF to lower velocities by treating the depinning of the CDW as a critical phenomenon. The model incorporates a CDW elasticity through the effective interactions J_{ij} between the phases ϕ_i and ϕ_j at impurity sites $\boldsymbol{R}_i$ and $\boldsymbol{R}_j$:

$$H_0 = -\sum_j h_j \cos(\phi_j - \beta_j) + \tfrac{1}{2}\sum_{ij} J_{ij}(\phi_i - \phi_j)^2. \tag{2.8}$$

The preferred phase at $\boldsymbol{R}_j$ is β_j and the pinning strength is h_j. For convenience the strength of the pinning potential is always the same: $h_j = h$. In the mean field (infinite range) approximation N phases are coupled by $J_{ij} = J/N$. The equation of motion is written

$$\frac{\mathrm{d}\phi_j}{\mathrm{d}t} = -\frac{\delta H_0}{\delta \phi_j} + F, \tag{2.9}$$

where the inertial term has been neglected and F is the driving field. The narrow-band noise amplitude is obtained from the velocity–velocity correlation function. As in critical phenomena, the appropriate length scale diverges at the transition between the moving and non-moving state,

$$\xi(F) \sim \xi_0 \left(\frac{F - F_T}{F_T}\right)^{-\nu}, \tag{2.10}$$

with F_T the threshold, ξ_0 the phase–phase correlation length, and $\nu = 1/2$ in the mean field calculation. The important result to emerge from the mean field calculation is the jerkiness of the motion on the length scale of $\xi(F)$. This result is surprising, because each phase is coupled to the mean velocity field,

$$\bar{\phi}(t) = \frac{1}{2N}\sum_j \phi_j(t), \tag{2.11}$$

so that eq. (2.8) is rewritten

$$H_0(MF) = \frac{J}{2N}\sum_j (\phi_j - \bar{\phi})^2 - \sum_j h_j \cos(\phi_j - \beta_j). \tag{2.12}$$

The equation of motion for the phase at the jth impurity is

$$\frac{d\phi_j}{dt} = J(\phi_j - \bar{\phi}) - \sum_j h_j \cos(\phi_j - \beta_j). \tag{2.13}$$

In the limit of an infinite number of impurities, we can write $\bar{\phi}(t) = vt$. Although far above threshold the motion of individual phases will be relatively smooth, at smaller electric fields the relative phase velocities become more 'jerky'.

Fisher argues that short-range interactions will only enhance the jerkiness of the motion. Far above threshold ξ is comparable to ξ_0, but closer to threshold ξ diverges according to eq. (2.10). Here as in the single-phase model, the CDW spends most of the time almost pinned (moving very slowly), then quickly advances a large fraction of 2π. The important consequence of the divergence is an enhanced ac noise amplitude near to the threshold

$$\langle j_{ac}^2 \rangle^{1/2} / j_{dc} \sim \left(\frac{F - F_T}{F_T}\right)^{\nu/2(d-4+\eta)} \left(\frac{\xi_d}{V}\right)^{1/2}. \tag{2.14}$$

Contained in eq. (2.43) is the volume incoherence factor $\langle j_{ac}^2 \rangle^{1/2} \sim V^{-1/2}$ that can be tested experimentally.

2.3. Current oscillations and microscopic pinning

Many of the attempts to determine the pinning forces on a microscopic level have been led by Zawadowski. Barnes and Zawadowski (1983) have calculated the effect of scattering of electron–hole pairs by impurities and implications for pinning of the CDW and narrow-band noise. Later, the interaction of the CDW and Friedel oscillations created near the impurity was investigated by Tutto and Zawadowski (1985) to higher orders in the perturbation. It is important to mention these results because any form obtained from the microscopic theory can in turn be used in the macroscopic equations of motion. For convenience, only a one-dimensional segment is considered and the phase is coherent over that segment.

The charge-density wave is formed by two macroscopic quantum states consisting of electron–hole pairs with momentum $\pm 2k_F$ and spin zero. It is the interference of the two states which results in the gap formation and thus the CDW. To second order in the acceleration (scattering) of the CDW by a single impurity, a transition takes place in which two electrons are scattered from the same side of the dispersion curve to the opposite. In turn, the position (phase) of the two states combine to form the CDW position $\phi = \phi_L - \phi_R$, and the transition rate depends on position as $\sin[2(\phi - \phi_0)]$, where ϕ_0 is the preferred position. Therefore, the scattering rate due to the impurity oscillates in time and may be a contributing source

of the oscillation phenomena. The second-order results predict a pinning wavelength that is half the CDW wavelength. If no more terms were important, the ratio of j_c/f_0 would be half that predicted from the phenomenological treatments above.

Higher-order processes are also possible, and it turns out significant. The origin of the terms comes from scattering of electrons that move in the effective potential induced by the CDW; they are shown in fig. 2.2. Perhaps an easier way to visualize the impurity pinning to nth order is to describe the interference between the charge-density wave and the Friedel oscillation formed about the impurity. The electron density is either maximal or minimal at the impurity, with periodicity $2k_F$ just as the CDW. The phase of the CDW is mismatched with the Friedel oscillation in general, so there must be a crossover region around the impurity (in a volume x_0).

Since the volume over which the amplitude can vary (ξ_0) usually satisfies $\xi_0 \gg x_0$, the phase on two sides of the impurity cannot change by much. Long-range deformations act to minimize the overall energy in the regions around the impurities. The effective potential V_0 at the impurity site can be borrowed from the microscopic description mentioned here and incorporated into any calculations using a phase Hamiltonian such as eq. (2.8). Tutto and Zawadowski predict that at temperatures close to the CDW phase transition the effective potential becomes more sinusoidal. Shown in fig. 2.3 is an example of the potential. The harmonic content of the NBN, as in the classical theories depends on the velocity; any shape of the potential gives 'spike-like' behavior very close to threshold. For overdamped motion at high velocities, it is the spatial derivative of the potential that directly gives the velocity and therefore the harmonic content. Sinusoidal behavior near T_p results from the higher-order perturbation terms exerting a force

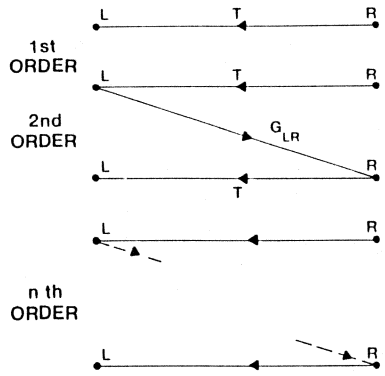

Fig. 2.2. Higher-order electron–hole scattering processes as described by Barnes and Zawadowski (1983).

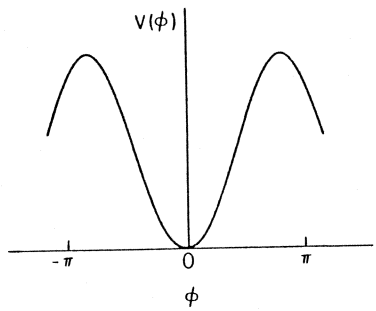

Fig. 2.3. Potential as created by impurities in the model calculated by Tutto and Zawadowski (1985).

on the CDW that decreases faster than the order parameter, which in turn determines the first-order term through, for example, Coulomb interactions.

2.4. The tunneling model and current oscillations

Bardeen (1985) has proposed a mechanism for CDW transport which involves the coherent macroscopic tunneling between two energetically equivalent states $\phi_A(x)$ and $\phi_B(x)$. One important difference between models described previously and the tunneling model is the alternation between the two states. In the presence of an electric field, a CDW in state ϕ_A will move from its optimal position at the average rate $-v_d t$. When the spatial average position is $\pi/2$, ϕ_A and ϕ_B are equivalent in energy but separated by a barrier. At phases $\phi > \pi/2$, ϕ_B is favorable. The effective potential, as shown in fig. 2.4, can be written

$$V(\theta) = \begin{cases} -\cos\theta, & -\pi/2 < \theta < \pi/2, \\ \cos\theta, & \pi/2 < \theta < 3\pi/2. \end{cases} \tag{2.15}$$

The CDW current is determined by the transition rate between the two states. The effective potential is similar in shape to that calculated by Tutto and Zawadowski (1985) but is shorter in spatial periodicity by a factor of two. Similar to the deformable classical models, it is the ability for the CDW to change its form to best accommodate the impurity potential that allows for sliding motion.

The motion of the CDW as described in the tunneling model can be discussed classically (Mihaly 1986) as illustrated in fig. 2.5 (using the strong pinning limit for convenience). Similar to the idealized case of Bardeen, place pinning centers an integral number of wavelengths apart at regular intervals. Halfway in between each of these, place another set of strong pinning centers. The phase distorts to accommodate the new centers and therefore the lowest energy state is that shown in fig. 2.5b. Application of

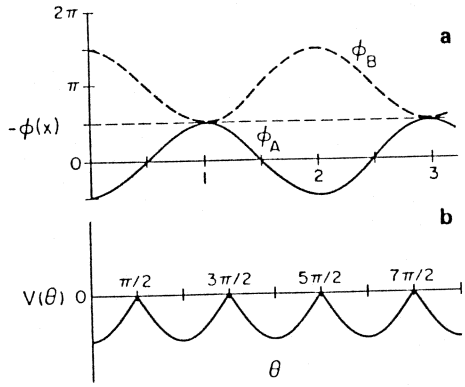

Fig. 2.4. (a) The two states ϕ_A and ϕ_B in the tunneling model. (b) Effective potential. Note that the periodicity is half that of classical pinning models (Bardeen 1985).

an electric field moves the compressed region to the position of fig. 2.5c, so that the CDW is always pinned at one half of the sites. The repetition of this process gives an average phase advance of π per cycle, as in the tunneling picture. Forcing the CDW to move in this manner retains the potential of eq. (2.15); the rich harmonic content of the oscillations persists to high fields. Similar to the classical phase treatments of CDW sliding motion, the

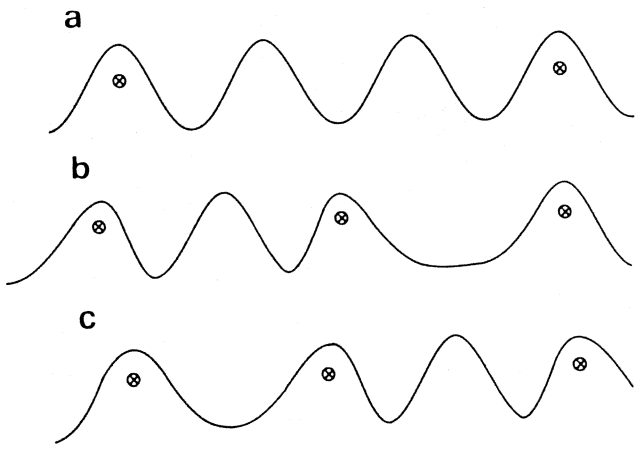

Fig. 2.5. Classical analogy to the tunneling model, strong pinning limit. (a) The CDW is pinned by two impurities an integral number of wavelengths apart. (b) Insertion of an impurity midway between causes a compression in one half and an extention in the other. (c) An electric field shifts the compressed region.

source of the narrow-band noise is a bulk phenomenon due to impurity pinning.

2.5. Phase-slip processes

All of the models described above have the common feature that the narrow-band noise arises from bulk pinning effects, so in that sense they are indistinguishable. However, because the ratio $\delta V / V_T$ is so small the connection is not straightforward; indeed, experiments addressing this issue are a main topic of this chapter. It can also lead one to search for other explanations regarding the source of the noise.

Up until now, only phase excitations have been considered. Amplitude fluctuations are completely neglected. In some limits this is acceptable, but at least in one case for every sample, amplitude excitations have to be included. In the presence of a very weak pinning center, the CDW phase will be distorted a small amount and the size of the gap will remain large; the density of condensed carriers remains constant near the pinning center. However, in the limit when a dislocation or chemical impurity has such a strong effect to completely block the sliding mode, then the order parameter will decrease near the impurity. The only way for current to pass is by normal single-particle transport.

This process must occur at the contacts for every sample. Ong, Verma, and Maki (1984) and independently Gor'kov (1983) have developed a theory describing the conversion of CDW carriers to normal carriers at the terminals of the sample. The spatially periodic charge modulation leads to the oscillating voltages picked up in the experimenters' detection circuits. Their proposal depends on the creation of an array of vortices at the sample ends, or anywhere there is a phase discontinuity. Included is the assumption that the static phase–phase coherence length is much shorter than any dynamical phase coherence lengths, which may be on the order of the total length of the sample. This supposition leads to a *uniform* CDW velocity in time and space in the bulk of the sample. The creation of vortices at one end of the sample and the annihilation at the other is the source of the ac conduction noise. Conservation of charge requires us to write

$$v_d l_v = v_s \lambda_{CDW}, \tag{2.16}$$

where l_v is the vortex spacing and v_s the velocity.

The phase-slip process can be thought of as the way the sample reduces stress that is built up by the dc electric field. The phase is considered to be fixed at the end of the sample. A sliding charge-density wave moving towards the contact tries to compress the CDW near the contact because of this boundary condition. By letting the phase change by an amount 2π the energy stored in the system is released, like shorting out a capacitor. The

amplitude fluctuations discussed earlier are from the requirement that the discharge be in the form of 'normal electrons', able to propagate outside of the sample into the measuring leads.

The current oscillations become a modulated chemical potential difference in the experiment through an effective resistance that is independent of sample length but inversely proportional to the sample width. **Therefore, it is expected that the voltage amplitude $U_0 \sim R_{\text{eff}}$.**

The important length scale in the vortex model is the distance over which the CDW velocity decreases to zero at the contact. We expect that the oscillations decay exponentially over the phase-slip length ξ; therefore the ac electric field is given by

$$E(x) = E_\omega(e^{-x/\xi} + e^{i\phi}\, e^{-(\ell - x)/\xi}), \tag{2.17}$$

where ϕ is the random phase between the noise sources at the two ends of the sample. Integrating eq. (2.17) over the length of the sample gives the total measured ac voltage.

3. *Experimental issues pertaining to the narrow-band noise*

Experimentalists have investigated several aspects of CDW motion via measurements of the oscillation phenomena and the related observations of the interference effects upon application of an ac electric field.

3.1. Volume dependence of the oscillations

One of the controversial issues is the origin of the oscillations and its relation to CDW motion, as discussed in section 2. The experiments can be divided into two classes: those that address the volume dependence and others where it is attempted to separate the signals coming from each end (for example, through the use of a temperature gradient). Here we discuss the results of three of those experiments as performed by Mozurkewich and Grüner (1983), Jing and Ong (1986) and Brown and Mihaly (1985).

First, however, it should be emphasized that these measurements are difficult to draw conclusions from. The reason is a lack of reproducibility that has been noted by several authors. The material of choice is $NbSe_3$ where the NBN peaks are extremely sharp, usually much less than 10 kHz wide. Typically the drive is a constant dc current and the voltage is measured as a function of time. This signal is in turn fed to a spectrum analyzer (different than a Fast Fourier Transform). The fundamental peak in the spectrum is arbitrarily selected for the measurements. It is assumed that any information contained in the higher harmonics is obtained by measuring the fundamental only and does not change from crystal to crystal.

The next difficulty arises from fluctuations in the spectrum. In the time domain a periodic signal that fluctuates considerably is observed. On the trace of a spectrum analyzer, the height of the peaks vary in time and the finite widths in frequency space also vary. A good simulation of the signal can be constructed by feeding a white noise source to the Voltage-Controlled Oscillator input of a function generator. The output of the generator looks similar to the response from a $NbSe_3$ crystal. When measuring the oscillations a bandwidth must be chosen along with a method for signal averaging. The choice of measurement bandwidth becomes significant when signal to noise ratios are marginal and when the fluctuations change from one experimental run to another.

Mozurkewich and Grüner (1983) tried to overcome these difficulties by keeping the measurement bandwidth larger than the signal and the fundamental centered around 10 MHz. In this way, they measured the root-mean-square (rms) voltage $V_{rms} \equiv \Delta V$ of the fundamental frequency peak. The dependence on cross-sectional area was made by applying two contacts to the sample and measuring. Then the contacts were removed and the sample was cleaved along the direction of CDW current. The process was repeated as many times as feasible. The length dependence was measured in a similar fashion except that the cuts were made orthogonal to the direction of current. Their results are summarized in fig. 3.1, where $\Delta j \equiv \Delta V/RA = \Delta V/\rho\ell$ is plotted versus sample volume (A is the cross-sectional area, ρ is the resistivity, and ℓ is the length of the sample). The quantity Δj is assumed to be the oscillating current that would be detected if the drive was voltage rather than current. Technically this is valid only for a non-

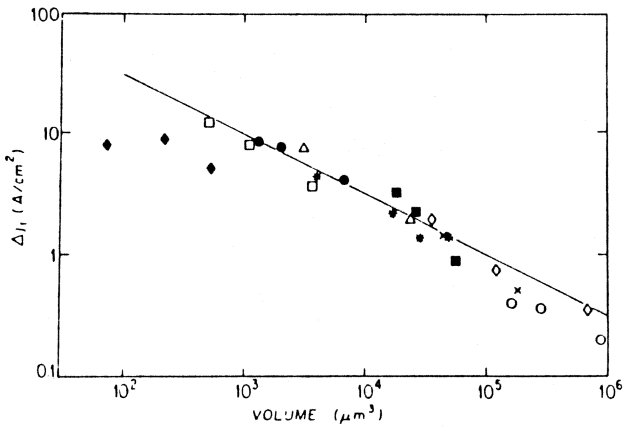

Fig. 3.1. Volume dependence of the amplitude of the fundamental oscillation frequency (Mozurkewich and Grüner 1983).

interacting two-fluid model (representing the CDW electrons and the 'normal' electrons). The solid line has a slope of $-1/2$, which would indicate a vanishing current oscillation amplitude in the infinite volume limit.

The $1/(\text{volume})^{1/2}$ behavior is the result one obtains for the two-dimensional random walk. Consider a circuit consisting of a string of independent ac voltage sources all of the same frequency and amplitude V_0. The rms voltage measured at the ends, because the relative phases are uncorrelated, is proportional to the square root of the number of oscillators N:

$$V_{\text{rms}} = V_0\sqrt{N}. \tag{3.1}$$

Normalizing to obtain the current and associating a length with each oscillator gives an ac current that varies as $1/(\text{length})^{1/2}$. Of course the damping must be included, so phenomenologically we associate a resistance that may be field dependent with each oscillator. Similarly, the cross-sectional area dependence can be modelled by placing oscillator–resistor pairs in parallel. In that case $\Delta j \sim \Delta V \sim 1/(\text{area})^{1/2}$. It was found using an overdamped oscillator model for the fit that the appropriate domain volume $V_d \geq 0.2\ \mu\text{m}^3$. It is possible that the domain volume depends on the CDW velocity, as described by Fisher (1985).

The measurements of Mozurkewich and Grüner remained controversial, as Ong, Verma and Maki (1984) presented a study that showed no length dependence at all, but with a considerable amount of scatter in the data. Brown and Mihaly (1985) attempted a different type of experiment, where the length dependence could be measured without cutting the sample. The main idea was to first make a contact to the sample that did not reduce the electric field in the sample very much directly under it. Usually, silver paste or some other conductor is used to make contact to the sample which reduces the electric field and therefore 'stops' the CDW in that region (Ong and Verma 1983). The required conversion to normal current is the process that generates the narrow-band noise in the contact models, thereby effecting the measurement. What they used was another $NbSe_3$ fiber that could be pressed lightly against the sample as a third contact, with the additional capability that it could be moved during the experimental run. The movable 'middle' contact allowed for three measurements to be made for each position: the voltage between both ends V_{13}, and the voltage from each end to the middle V_{12} and V_{23}. The results from that experiment are shown in fig. 3.2. Data taken from three samples are shown in the figure, for which the lengths varied 0.6–1.1 mm. The length is normalized to one, and the position of the middle contact is the distance between contacts 1 and 2. The general trend is that the noise amplitude increases with contact separation, but not in a linear fashion. In fact, the results are consistent with the model described above by the string of random-phase oscillators. For entirely random phases, one expects $(V_{12} + V_{23})/V_{13} = \sqrt{2}$ when contact 2 is

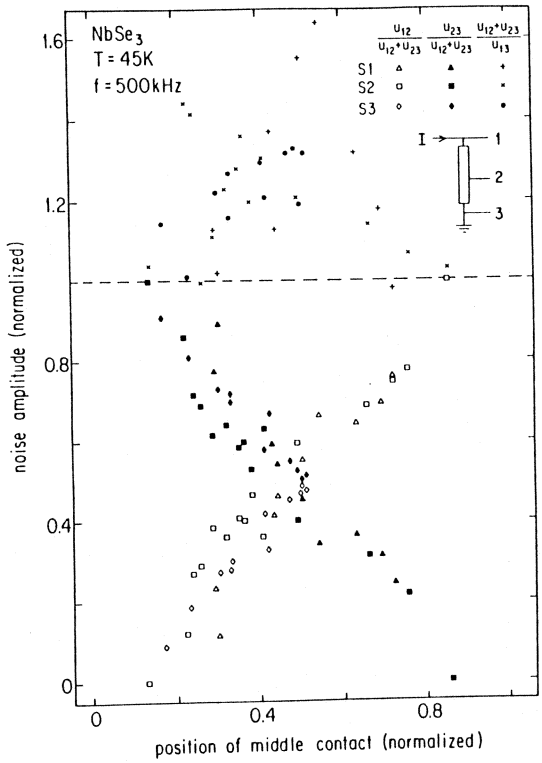

Fig. 3.2. Noise amplitude versus position of the middle contact. The solid symbols represent the signal between contacts 2 and 3 (inset) and the open symbols are between contacts 1 and 2. Also plotted is the sum (above the dashed line) (Brown and Mihaly 1985).

at the center of the sample. The hypothesis that the voltage oscillations are generated in the bulk of the sample is further supported by their observation of the relative phase of the narrow-band noise on the two sides of the sample. Brown and Mihaly (1985) reported that there was no observable correlation, indicating a fluctuating relative phase on a very fast time scale.

The study was extended to include samples of a broader range in length (up to 1.7 mm long), with the results plotted in fig. 3.3. Fits were generated using eq. (2.17) of the vortex model for each sample with a constant $\xi = 0.3$ mm, and the phases of the oscillations at each end are random and fluctuating. The dashed line is a fit to the random-phase oscillator model. From the three plots, it is clear that the only way to consistently explain the results using the contact description is to keep the ratio ξ/ℓ a constant (solid line). Physically, ξ represents the appropriate length scale for screening of the vortex array, and reflects the velocity correlation function. As

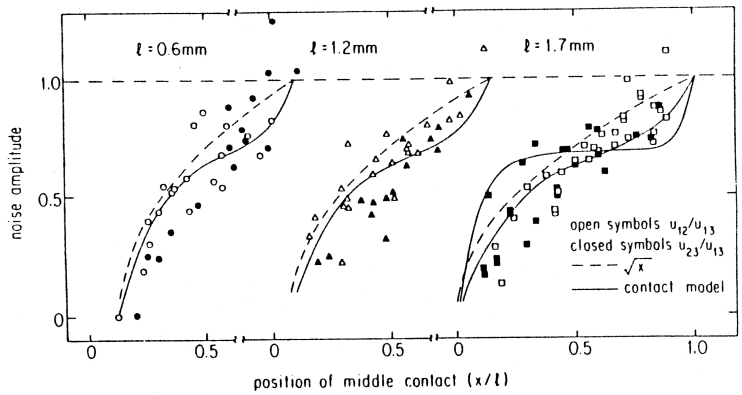

Fig. 3.3. Noise amplitude versus position of middle contact. The signal from the two sides of the sample are plotted on top of each other for convenience. The dashed lines are a fit to the random-phase oscillator model. The solid lines are a fit to eq. (2.17) with ξ/ℓ = constant. The longest sample also has been fit with $\xi = 0.3$ mm.

discussed by Fisher (1985), the velocity correlation length is larger than the Lee–Rice phase coherence length. Also, since the velocity is zero at the contact, it is the small velocity length which is important. There is no reason why ξ should change with sample length when $\ell > \xi$. In all of the experiments this condition should hold, since the shortest sample for which we have a fit $\xi \sim 0.3$ mm, with no phase coherence to the oscillations between the two sides of the sample.

More recently, Jing and Ong (1986) have reported a length dependent ac amplitude that indicates $\xi \sim 0.26$ mm. It appears difficult to simultaneously explain the results from the two experiments. However, we point out that there are some indications from experiments performed in the presence of a temperature gradient that the noise generation is a phenomenon resulting from bulk pinning of the charge-density wave (Lyding et al. 1986).

3.2. *Periodicity of the potential*

Provided that the narrow-band noise actually reflects bulk pinning, one can learn something about the effective potential by studying the harmonic content of the oscillatory response and from the constant ratio of excess current density to fundamental frequency f_0.

As presented in section 2, the time-average current density j_{CDW} is

$$j_{CDW} = n_{CDW} e \lambda f_0, \tag{3.2}$$

where n_{CDW} is the density of the condensed electrons and λ is the effective pinning wavelength. The density can be considered to be an order

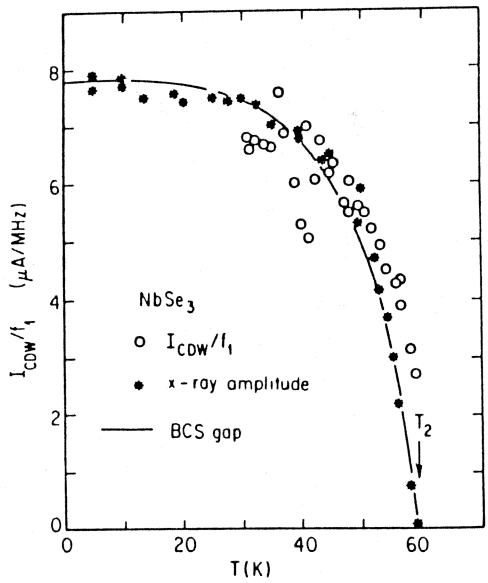

Fig. 3.4. Ratio I_{CDW}/f_0 versus temperature for $NbSe_3$ (open circles (Zettl and Grüner 1985)) and compared to the X-ray data of Fleming et al. (1978).

parameter as demonstrated by Zettl and Grüner (1984) and illustrated in fig. 3.4. The open circles are I_{CDW}/f_0 directly, and the asterisks are taken from X-ray diffraction experiments (Fleming et al. 1978) (the intensity of the satellite peaks). Normalizing the current to a single chain gives

$$j_c = q \quad \text{per chain,} \tag{3.3}$$

where q is the net charge transported per chain per ac cycle. Experimentally, this number has been controversial for various reasons. First, the number of condensed electrons in $NbSe_3$ for each CDW is not known. The semiconducting materials are more difficult to get clean measurements from, because typically there is a significant spread in the fundamental frequency (indicating a corresponding distribution of CDW velocity in the sample). Plots constructed from CDW current and fundamental frequency where there are such distributions are not linear (Brown et al. 1985). This effect is illustrated in fig. 3.5, where at $T = 164$ K for this orthorhombic TaS_3 (o-TaS_3) sample there is a pronounced curvature. However, the slope tends toward a constant as the frequency is increased. Also plotted is the same quantity, but using the interference phenomena (Shapiro steps) as frequency markers (recall that steps are observed in the I–V curve whenever the NBN frequency is an integer multiple of an external drive

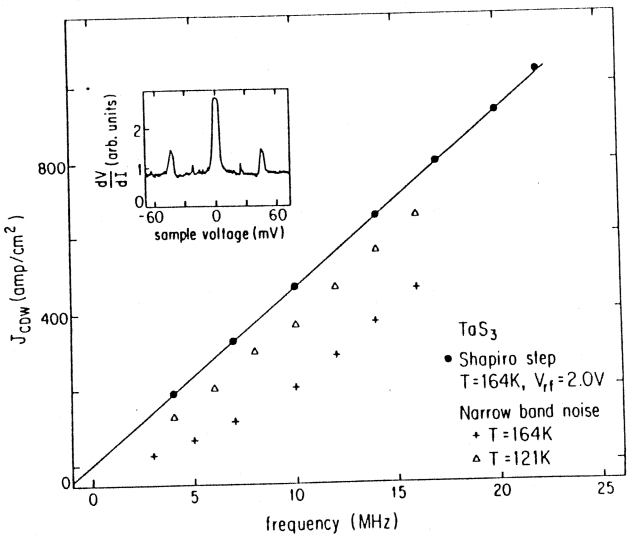

Fig. 3.5. Excess current versus fundamental oscillation frequency in TaS_3. The (+, Δ) symbols are taken from direct measurements of the oscillations. The solid circles are from the Shapiro steps.

frequency). The data fit an excellent straight line with intercept at zero, as would be expected for a coherent sample response.

Because the Shapiro step curve and the NBN curve do not coincide, the CDW current at a step should depend on the rf power applied. This can be understood, if, for example, there is a distribution of threshold fields within the sample. The large amplitude ac may act to reduce the importance of that distribution for at least two possible reasons. If the significant parameter is $E - E_T$, then sufficiently large fields reduce the importance of a distribution of E_T. For some samples, the steps are observed to become sharper with increased amplitude of the ac driving field, indicating increased synchronization of the sample response.

Electron diffraction experiments (Wang et al. 1983) show that the temperature dependence of the superlattice wavevector is weak, and therefore any observed temperature dependence of the slope j_{CDW}/f_0 can be attributed to a change in the CDW electron density $n(T)$. The results from the temperature dependence study appear in fig. 3.6, showing almost no change over the range 115–200 K. Above 200 K the value drops quickly towards zero as the transition temperature $T_p \sim 220$ K is approached. Compared to similar results for $NbSe_3$, the development of the order parameter occurs over a much smaller range in temperatures (non-BCS behavior). It may be a result of the more one-dimensional nature of TaS_3 that the mean-field theory is less appropriate.

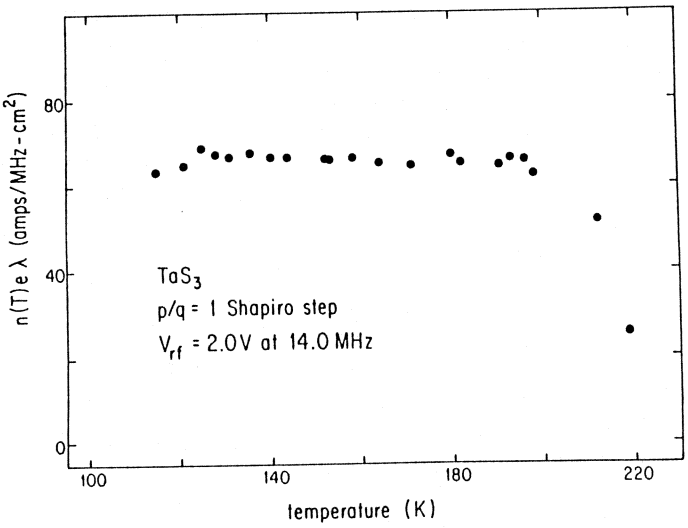

Fig. 3.6. Temperature dependence of the ratio J_{CDW}/f_0.

Evaluation of the temperature independent region gives

$$j_c/f_0 = (2.0 \pm 0.2)e, \tag{3.4}$$

consistent with those models where the energy periodicity related to the phase of the condensate is just the wavelength of the CDW distortion. The issue is not considered closed because estimates from other materials disagree. Recent measurements (Hundley et al. 1988) in the blue bronze $K_{0.3}MoO_3$ are consistent with that reported here. However, the semimetals $NbSe_3$ and monoclinic TaS_3 seem to yield results more consistent with a pinning wavelength that is half of the CDW wavelength (Monceau et al. 1983).

3.3. Statistical measurements of the narrow-band noise

We mentioned earlier the difficulty of doing measurements of the NBN because of fluctuations in the detected signal. Link and Mozurkewich (1988) performed a statistical study of those fluctuations and found the distribution of voltages corresponding to the fundamental frequency to be Gaussian in shape and centered about zero. This is the same distribution one obtains for Johnson noise in resistors. There is a time scale which serves as a crossover to the Gaussian behavior; when the voltages are recorded over a short enough interval, a bimodal distribution, as in fig. 3.7, is observed. Link and Mozurkewich found the crossover time τ to the Gaussian shape to be as short as 10 μs. When continually longer intervals are

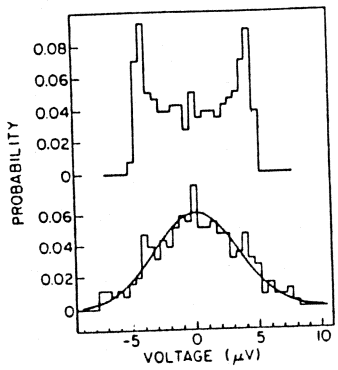

Fig. 3.7. Histograms of the voltage response of $NbSe_3$ above threshold. At short times the structure is bimodal (top), whereas longer records reveal the unimodal shape (bottom) (Link and Mozurkewich 1988).

used the distribution becomes unimodal, with τ varying from record to record. It is possible the variation is a result of finite-size effects. It was demonstrated in a study of the fluctuations in the higher harmonics of the NBN that the fundamental and first harmonic signals are uncorrelated. This may be considered surprising because empirically the spectral widths of the various harmonics scale with each other.

Their observations put constraints on possible models for the noise generation. Any model with a unique sliding state can be eliminated. One possibility is to allow the relative phase among various regions of the sample to vary (Brown et al. 1985). We note, however, that various aspects of pinning in sliding CDW systems are not understood, since none of the available calculations of the phase Hamiltonians reproduce the fluctuations.

4. *Electronic interference effects*

The coexistence of an intrinsic narrow band noise frequency and the inherent nonlinear CDW I–V characteristic sets the stage for a number of spectacular electronic interference effects in sliding CDW conductors. The CDW may be driven by an electric field of the form

$$E = E_{dc} + E_{ac}P(t), \tag{4.1}$$

where E_{dc} represents a dc bias offset and E_{ac} is the amplitude of the ac component $P(t)$. In practice, the drive is more often a total current, similar in form to eq. (4.1). In either case, the system response is not a smooth function of the drive parameters, but shows anomalous 'interference' structure. The response is determined by measuring the current through (or

voltage across) the sample. The response signal may be viewed in real time (as in pulse synchronization and transient ringing experiments), viewed in the frequency domain (as in frequency locking and chaos experiments), or filtered for a single frequency (as in ac conductivity measurements and dc $I-V$ curves). In all cases, interference usually occurs whenever the internal narrow band noise frequency ω_{NBN} is equal to or simply related to a characteristic frequency of the ac drive. $P(t)$ is a periodic function of time t and may, for example, be a sinusoid, square wave, or train of rectangular pulses. In $NbSe_3$, TaS_3, and $K_{0.3}MoO_3$, interference has been observed in the dc conductivity (Monceau et al. 1980, Brown et al. 1985, Zettl and Grüner 1983, Hall and Zettl 1984, Brown et al. 1984, Sherwin and Zettl 1985, Thorne et al. 1987, Hundley and Zettl 1988), ac conductivity (Zettl and Grüner 1984, Cava et al. 1984, Hundley and Zettl 1988), and real time transient response (Fleming 1982, Brown et al. 1986, Fleming et al. 1985). $NbSe_3$ shows the strongest interference effects, presumably because the CDW response is most coherent in that material.

4.1. Shapiro steps

One of the most dramatic CDW interference effects and the one emphasized in this review is a modification of the sample $I-V$ characteristics in the presence of a superposed ac drive field. In the most common experimental situation, the ac field is a sinusoid and hence the total applied field is of the form

$$E = E_{dc} + E_{ac}\cos(\omega_{ex}t). \tag{4.2}$$

Under these conditions, anomalies occur in the dc $I-V$ characteristics whenever the narrow band noise frequency and applied frequency are related by

$$\omega_{NBN}/\omega_{ex} = p/q, \tag{4.3}$$

with p and q integers. Figure 4.1 shows an early observation (Monceau et al. 1980) of such interference in the differential resistance of $NbSe_3$. The sharp spikes in dV/dI occur when $\omega_{NBN}/\omega_{ex} = 1$, 2, 3, etc. Similar interference is obtained in TaS_3 (Brown et al. 1985) and $K_{0.3}MoO_3$ (Hundley and Zettl 1988). Figure 4.2 shows that the interference peaks in dV/dI correspond to actual 'steps' in the direct $I-V$ characteristics (Zettl and Grüner 1983). The magnitude of the steps, δV, is a strong function of external ac frequency and amplitude. The steps observed in CDW materials are similar to those observed in the $I-V$ characteristics of dc biased Josephson junctions in the presence of microwave radiation, as originally studied by Shapiro (1963). In the Josephson junction case, the steps reflect interference between the internal ac Josephson oscillations and the exter-

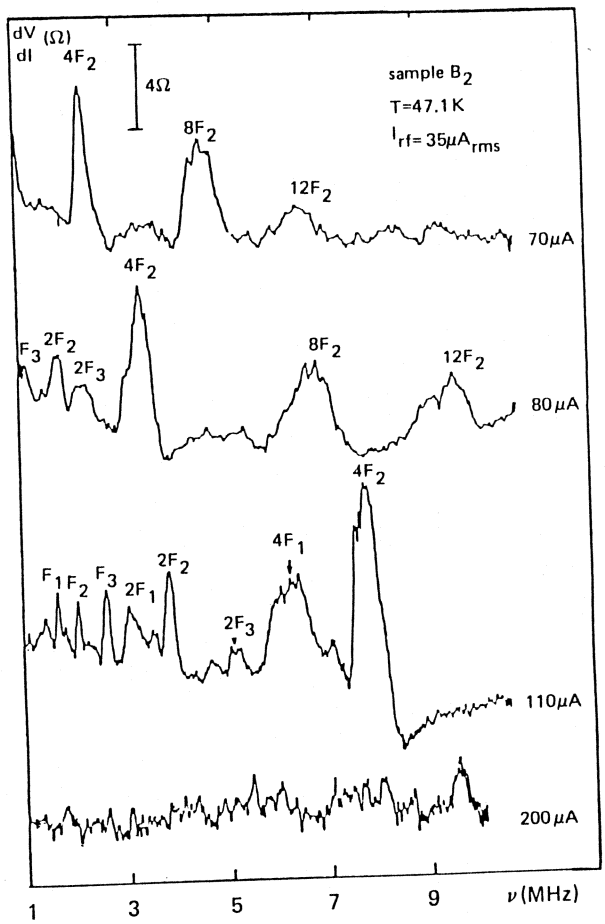

Fig. 4.1. Differential resistance in $NbSe_3$ measured in the presence of a superposed rf electric field. The sharp peaks represent interference structure. (From Monceau et al. 1980.)

nally applied microwave oscillations. Both the Josephson interference and CDW interference steps have become known as 'Shapiro steps'.

Similar interference effects are also observed in the dc $I-V$ characteristics of type II superconductors with flux vortex flow in the presence of rf radiation (Fiory 1971). Indeed, the close analogy between flux flow in superconductors and CDW motion, together with the previous observation of interference effects in type II superconductors, provided initial motivation for study of interference effects in $NbSe_3$.

Steps corresponding to integral values of $n \equiv p/q$ (eq. (4.3)) are commonly referred to as harmonic steps, while steps corresponding to non-

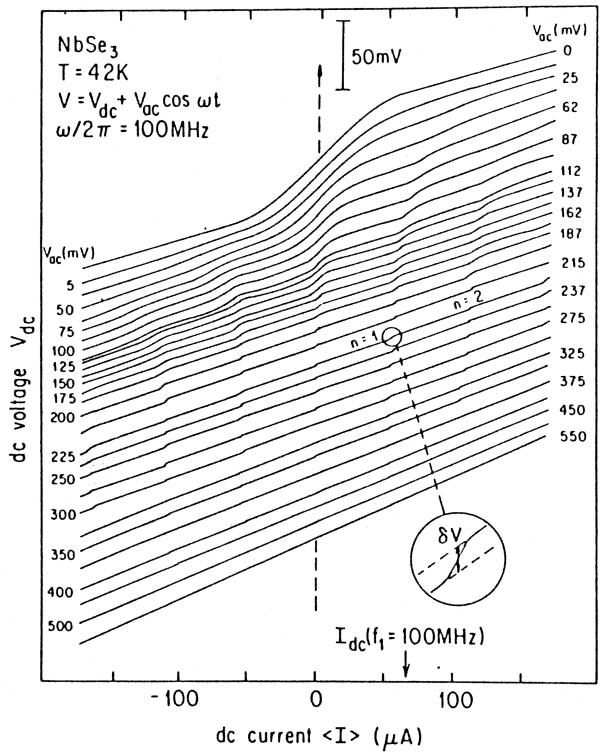

Fig. 4.2. Shapiro steps in direct $I-V$ curves of $NbSe_3$. The inset defines the step height δV. (From Zettl and Grüner 1983.)

integral n are referred to as subharmonic steps. Although early reports of Shapiro step interference in $NbSe_3$ made note (Monceau et al. 1980, Zettl and Grüner 1983) of the presence of subharmonic steps, more careful differential resistance measurements on CDW systems have since demonstrated an astoundingly rich subharmonic spectrum (Hall and Zettl 1984, Brown et al. 1984, Thorne et al. 1987). It is not uncommon to observe as many as 50 to 100 subharmonic steps between successive harmonic steps. Figure 4.3a shows a typical dV/dI interference plot for $NbSe_3$, with some dominant interference peaks identified with p/q values (Hall and Zettl 1984). The interference pattern displays self-similar structure, suggestive of fractal geometry (see section 5.1). Figures 4.3b,c show Shapiro step dV/dI plots for TaS_3 and $K_{0.3}MoO_3$, respectively (Brown et al. 1985, Hundley and Zettl 1988). Similar peak structure is observed, though the peaks are less sharp and smaller in relative height than those seen in $NbSe_3$.

Figure 4.3a shows that for the dominant interference peaks in $NbSe_3$, the

differential resistance dV/dI is flat over a substantial range of dc bias and achieves nearly the pinned, zero bias value. The CDW condensate is *mode locked* (Hall and Zettl 1984, Sherwin and Zettl 1985) during the interference, and does not contribute to the differential conductance of the sample (i.e. during mode locking only the normal, uncondensed electrons respond to small low-frequency ac perturbations of the electric field drive). The fact that dV/dI remains flat over a range of dc bias implies that near the step edges ω_{NBN} is pulled substantially away from its 'natural' value. The Shapiro step width or magnitude δV is a measure of over what range ω_{NBN} will track ω_{ex} due to mode locking. In an experimental dV/dI versus

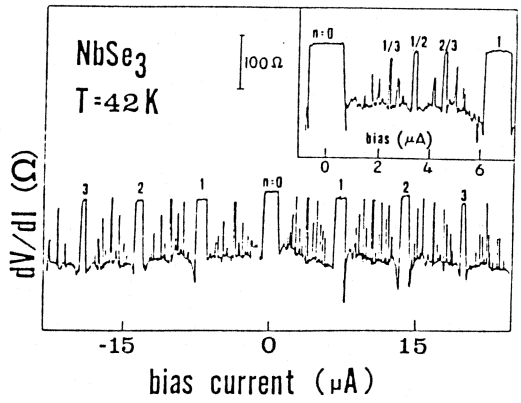

(a)

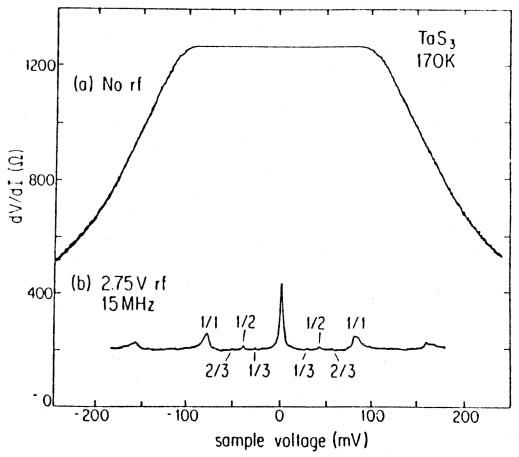

(b)

Fig. 4.3a,b.

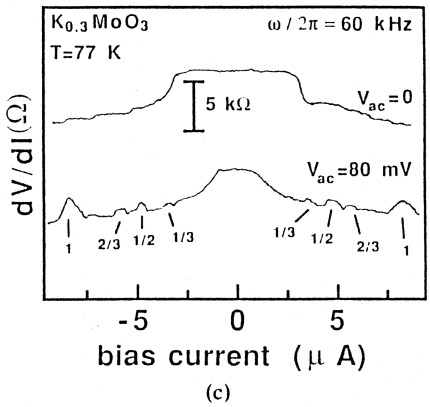

(c)

Fig. 4.3. (a) Shapiro step interference in dV/dI traces of $NbSe_3$. $n = p/q$ is the step index. The inset identifies some subharmonic steps. (From Hall and Zettl 1984.) (b) Harmonic and subharmonic Shapiro step interference peaks in TaS_3. (From Brown et al. 1985.) (c) Harmonic and subharmonic Shapiro step interference peaks in $K_{0.3}MoO_3$. (From Hundley and Zettl 1988.)

I_{dc} (*not* E_{dc}) plot, δV is found by integrating the area under the rectangular interference peak. Experimentally (Zettl and Grüner 1983, Thorne et al. 1987), δV is a strong function of the ac drive amplitude E_{ac} and frequency ω_{ex}. Figure 4.4 shows δV versus E_{ac} for the $n = 1/1$ Shapiro step in $NbSe_3$. For low values of E_{ac}, δV increases rapidly with increasing E_{ac}, but at higher ac drive oscillatory behavior is obtained.

As is to be expected, Shapiro step interference in the dc I–V characteristics similar to that shown in figs. 4.1 to 4.3 (sinusoidal drive) also occurs for non-sinusoidal ac excitation (Brown et al. 1986). Figure 4.5 compares dV/dI of $NbSe_3$ measured in the presence of a low-frequency sinusoidal drive with dc bias (upper trace), to that measured in the presence of a low-frequency square wave drive with dc bias (lower trace). For relatively large dc bias values, the two interference date sets look very similar. On the other hand, for very low values of E_{dc}, the square wave drive data shows suppressed interference peaks.

A more interesting situation occurs (Brown et al. 1986) if the square wave drive is asymmetric, as shown in fig. 4.6. In this drive configuration, the sample spends a waiting time t_1 below threshold and a time t_2 above threshold. The dc bias is defined as the time averaged response voltage measured experimentally. The inset to fig. 4.7 shows a typical dV/dI interference plot thus obtained (with the sample actually current, not voltage, driven). The interference peaks are closer together on the negative bias side, where the system spends a longer time above threshold. The

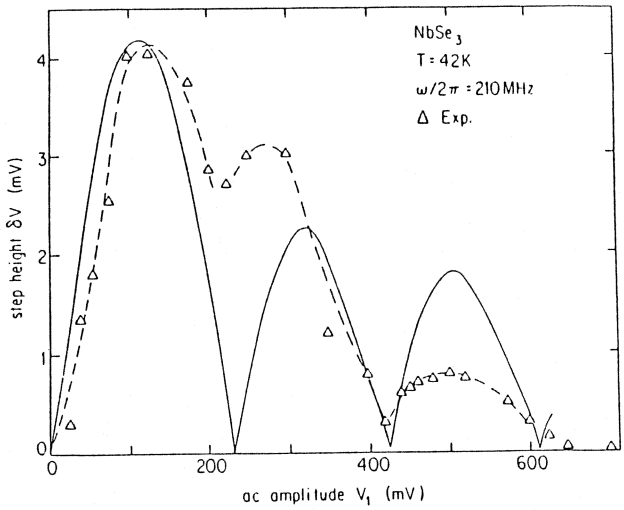

Fig. 4.4. Alternating current amplitude dependence of Shapiro step height δV in $NbSe_3$. The dashed lines are a guide to the eye for the experimental data. The solid line is eq. (4.9). (From Zettl and Grüner 1983.)

Shapiro step width δV is plotted in fig. 4.7 for different ac drive amplitudes and different t_1 and t_2 values. For short t_1, δV increases roughly linearly with t_1 and the relative slope of δV versus t_1 varies approximately as $1/t_2$. Saturation of δV occurs for large values of t_1.

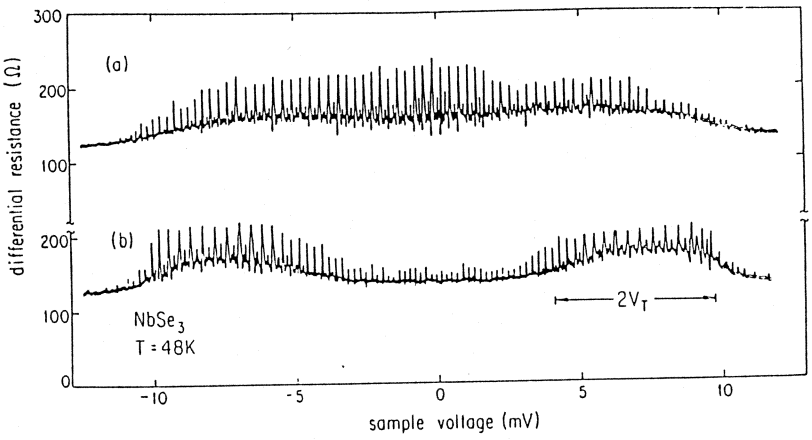

Fig. 4.5. Shapiro step interference in $NbSe_3$ for (a) sinusoidal ac drive and (b) square wave drive. The ac amplitude and frequency are identical in both traces. (From Brown et al. 1986.)

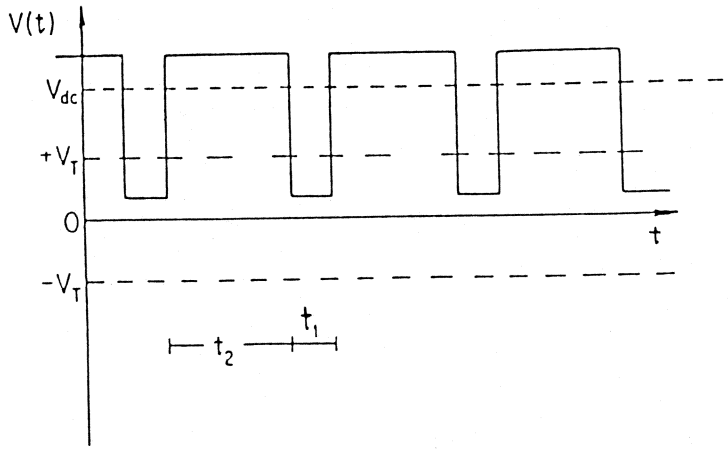

Fig. 4.6. Representative drive waveform for non-sinusoidal Shapiro steps experiments. (From Brown et al. 1986.)

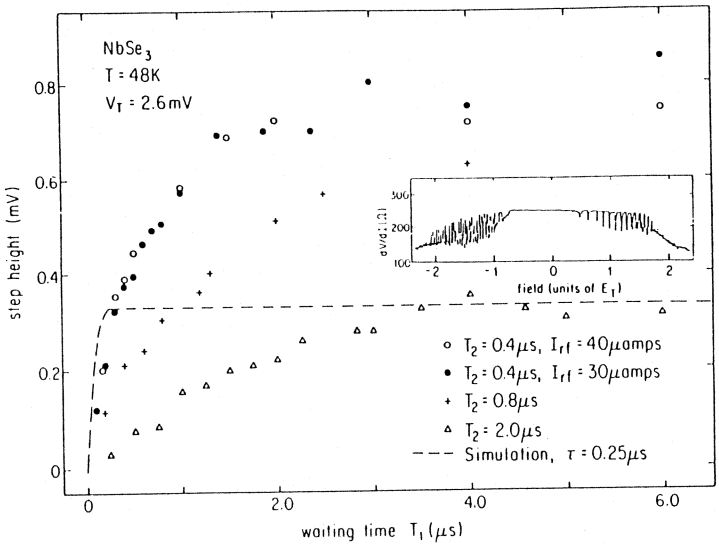

Fig. 4.7. Shapiro step magnitude in $NbSe_3$ for non-sinusoidal and non-symmetric ac drive. The times T_1 and T_2 correspond respectively to t_1 and t_2 in fig. 4.6. The dashed line is the prediction of eq. (4.6). The inset shows a typical Shapiro steps dV/dI trace for this type of ac drive. (From Brown et al. 1986.)

4.2. Single degree of freedom models for the interference

In a single-particle picture, Shapiro step interference and mode locking can be described in very simple terms. We first consider the motion of a charged particle in a periodic (e.g. sinusoidal) pinning potential. The most elementary electric field drive that satisfies eq. (4.1) is one where E switches periodically between two constant levels: $E = E_2 > E_T$ for a time duration t_2, followed by $E = E_1 = 0$ for a time duration t_1 (see fig. 4.6). In this special case, the particle begins to move from the bottom of a potential well when E_2 is applied. Provided the t_2 is sufficiently long, the particle will move out of the original well and into the next, or a more distant, well. After the field switches off to $E_1 = 0$, the particle relaxes to the bottom of the nearest well and remains there for the remainder of time t_1, until the field switches once again to E_2, etc. In the steady state, the ac-sensitive time averaged CDW current will be (Brown et al. 1986)

$$\langle j(t)\rangle \approx p\lambda/(t_1 + t_2), \tag{4.4}$$

where p is an integer and λ is the periodicity of the pinning potential. The dominant frequency of the external ac drive corresponds to a time period $(t_1 + t_2)$, hence we identify $\omega_{ex}/2\pi = (t_1 + t_2)^{-1}$. Together with eq. (4.4), this implies

$$\langle j(t)\rangle \approx p\lambda\omega_{ex}/2\pi, \tag{4.5}$$

i.e., the CDW current is locked to ω_{ex} and hence the particle is mode locked. A similar situation will occur even if $E_2 \neq 0$, since this simply redefines the dynamic minimum in the potential. An alternative but equivalent description of the locking involves energy considerations (Thorne et al. 1986). With only a dc bias applied above threshold, the moving particle has a potential energy that corresponds to its average height in the well. For the case of a sinusoidal pinning potential this will be halfway up the well. When the particle becomes phase locked, more time will be spent near the potential minima and the mean potential energy will decrease. This is a more favorable dynamic situation.

In the interference data of fig. 4.5, there is a strong cutoff for the interference at approximately ±10 mV dc bias, for both sinusoid and square wave ac drive. This cutoff corresponds to the situation where the drive signal no longer goes below threshold at any instance. This suggests that for Shapiro step interference to occur, the CDW system must spend some time below threshold during any one period of the ac drive. Further evidence for this is observed in the square wave data, for dc bias between approximately −4 mV and +4 mV. Here the external drive switches the sample between levels that are both larger than the threshold for depinning, but with opposite signs. Hence for this set of drive parameters the sample spends

virtually no time below threshold, and the Shapiro step interference is greatly suppressed. The corresponding sine wave drive data shows no such suppression, because for a sinusoidal drive of similar amplitude there is always a non-negligible time spent below threshold.

In the case of rectangular pulse ac drive with two relevant times t_1 and t_2 (see fig. 4.6), a single-particle calculation yields for two limiting cases the following expressions for the Shapiro step magnitude (Brown et al. 1986):

$$\delta V = V_T \tau / t_2, \qquad t_1 \gg t, \tag{4.6a}$$

$$\delta V = 2 V_T t_1 / t_2, \qquad t_1 \ll \tau, \tag{4.6b}$$

where τ is the CDW damping time. Equations (4.6a,b) are independent of the specific form of the pinning potential. Physically, the forms of eqs. (4.6a,b) can be understood by considering t_1, the time spent below threshold. When t_1 is long, the CDW current is always locked because a minimum in the potential can always be reached. For large E_{ac}, the steps will be equal in size and fill the E_{dc} axis, which means the step magnitudes vary as $1/t_2$. In the limit $t_1 \ll \tau$, the step width is limited by t_1.

Figure 4.7 shows as a dashed line the behavior predicted by this simple single-particle description. A fit to the data of δV versus t_1 at long t_1 yields $\tau = 0.25$ μs (eq. (4.6a)). At short t_1, the fit is not quantitatively consistent with experiment.

It should also be noted that recent Shapiro step interference experiments (Thorne et al. 1987) on $NbSe_3$ in the upper CDW state have demonstrated that, for samples with unusually sharp breaks in the $I-V$ characteristics at threshold (measured in the absence of rf radiation), Shapiro step interference with complete mode locking *does* obtain at high frequencies even if the CDW is never driven into the pinned state. It would appear inconsistent to describe these results in terms of a slow relaxation to the pinned state. Whether the unusual dc $I-V$ characteristics of these samples (suggestive of switching behavior, see below) is related to this 'enhanced' mode locking, is not clear.

We now examine more closely the case of sinusoidal ac drive fields where $E = E_{dc} + E_{ac}\cos(\omega_{ex} t)$. The highly oversimplified model of 'rigid' classical CDW motion described by the damped pendulum equation (Grüner et al. 1981)

$$d^2x/dt^2 + \tau^{-1}\, dx/dt + Q^{-1}\omega_0^2 \sin(Qx) = eE/m^*, \tag{4.7}$$

and introduced in section 2.1 is here surprisingly successful in providing qualitative and even quantitative fits to many features of the Shapiro step interference. In dimensionless form eq. (4.7) reads (Zettl and Grüner 1983)

$$d^2\theta/dt^2 + G\, d\theta/dt + \sin\theta = E/E_T, \tag{4.8}$$

where $G = (\omega_0 \tau)$ and time is measured in units of ω_0^{-1}. Equation (4.8) is well

known in the Josephson junction literature (Lindelof et al. 1981), where it describes the phase difference between superconductors comprising a resistively shunted junction (RSJ). In the current-driven Josephson junction case, E/E_T is replaced by I/I_T, and G is related to junction resistance R, capacitance C, and plasma frequency ω_J by $G=(RC\omega_J)^{-1}$. In the overdamped and high-frequency limit ($\omega_{ex} \gg \omega_0^2\tau$), eq. (4.8) predicts Shapiro steps in the $I-V$ characteristics whose magnitude for the $n=1/1$ step is given (Zettl and Grüner 1983) by

$$\delta V = 2\alpha V_T(\omega=0)|J_1(\omega_0^2\tau E_{ac}/\omega_{ex}E_T(\omega=0))|, \tag{4.9}$$

where α represents the CDW volume fraction locked to the external signal and J_1 is the first-order Bessel function. In the low-frequency limit ($\omega_{ex} \leqslant \omega_0^2\tau$), a modified Bessel-like solution for δV can be obtained numerically (Fack and Kose 1971). In the extreme low-frequency limit ($\omega_{ex} \ll \omega_0^2\tau$), the numerical solution predicts that δV has a maximum at $E_{ac}=E_T$ where $\delta V=(\omega_{ex}/\omega_0^2\tau)V_T$.

The solid line in fig. 4.4 is the prediction of eq. (4.9) for δV versus E_{ac}, with no fitting parameters except for α, which sets the vertical scale (in fig. 4.4, $\alpha=0.6$, suggesting for this sample 60% volume phase coherence). Although the fit in fig. 4.4 is surprisingly good, lending credibility to eq. (4.8), there are notable discrepancies between the Shapiro step data and the predictions of eq. (4.8). First, δV is predicted to vanish at the zeroes of J_1, while the experimental data suggest finite δV for all finite E_{ac}. This is shown more clearly in fig. 4.8. A second and perhaps more serious difficulty is that in the overdamped limit eq. (4.8) predicts no subharmonic interference. In $NbSe_3$, TaS_3 and $K_{0.3}MoO_3$ the ac conductivity suggests overdamped behavior, yet subharmonic Shapiro step interference is consistently observed. Hence, single-particle rigid motion in a sinusoidal potential cannot account for all aspects of Shapiro step interference.

The simplest correction to the deficiencies of eq. (4.7) or (4.8) is to retain the general form of the equation of motion but introduce a non-sinusoidal pinning potential. The expression for the Shapiro step magnitude then becomes (Thorne et al. 1987)

$$\delta V = V_T(\omega_{ex}=0)\,\mathrm{Max}_\theta\left\{2\sum(q\beta)a_qJ_p[q\beta\omega_1/\omega_{ex}]\sin(q\beta\theta)\right\}, \tag{4.10}$$

where $(q\beta)a_q$ is the qth Fourier component of the pinning force, J_p is the pth-order Bessel function, ω_1 is proportional to E_{ac}, and β is 1 or 2 for pinning periodicities 2π or π, respectively. Higher harmonics in the non-sinusoidal pinning potential lead to subharmonic interference steps, and the summation of Bessel functions in eq. (4.10) eliminates zeroes in the predicted δV, consistent with experiment. However, as shown in fig. 4.8, detailed measurements of δV versus E_{ac} on $NbSe_3$ samples indicate that δV exhibits

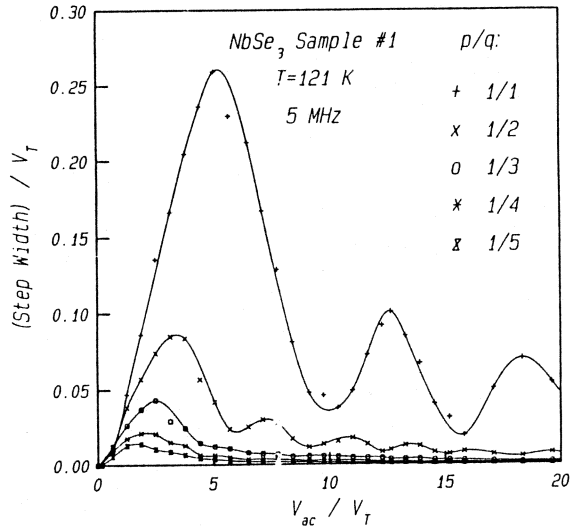

Fig. 4.8. Shapiro step magnitude versus ac drive amplitude in upper CDW state of $NbSe_3$. (From Thorne et al. 1987.)

smooth minima with increasing E_{ac}, while eq. (4.10) predicts sharp downward pointing cusps at the minima. This problem is generic to rigid particle classical models, regardless of the form of the pinning potential. In terms of generating narrow band noise spectra and harmonic and subharmonic Shapiro step interference most consistent with experiment, the best single-particle periodic potential appears to be cusped (Thorne et al. 1987), similar to that discussed by Tutto and Zawadowski (1985) and predicted by Bardeen's tunneling model (Bardeen 1985).

In Bardeen's tunneling model discussed previously in section 2.4, the electrons and macroscopically occupied phonons in the CDW are treated as a macroscopic quantum system with only one thermal degree of freedom in a large phase-coherent volume. The model is consistent with narrow band noise generation and nonlinear CDW $I-V$ characteristics and should, therefore, account at least to first order for Shapiro step interference. However, no specific form for δV or subharmonic interference structure has been calculated for the tunneling model.

4.3. Internal modes and relevant time scales

An increasing number of transport, structural, and NMR experiments on CDW conductors suggest that CDW internal degrees of freedom play a

central role in CDW dynamics. We will examine the relevance of internal modes to electronic interference effects.

Below threshold, the pinned CDW displays rich metastable state structure with both short and long characteristic time scales for decay. The long time scales can be on the order of thousands of years for a true equilibrium state to be reached. Metastable states correspond to different local configurations of CDW phase which results from the interaction of the condensate with crystal impurities. The states may correspond to an extremely polarized CDW, where the Q-vector (and hence single-particle gap) varies significantly over the length of the crystal.

Metastable state structure is well demonstrated by the so-called pulse-memory effect, first observed in $NbSe_3$ by Gill (1981) and subsequently identified in other CDW materials (Janossy et al. 1985, Fleming and Schneemeyer 1983). The effect is observed by exciting the CDW with a series of rectangular current pulses. If the amplitude of the pulses I_p exceeds the threshold I_T, then during the time between pulses the static CDW 'remembers' the polarity of the previous pulse. If a particular current pulse is of opposite polarity to the previous pulse, the voltage response of the system shows a slow 'charging' transient. This transient is interpreted as reflecting the nonequilibrium metastable state induced by repeatedly driving the CDW above threshold and quenching it to rest. As the CDW is excited by a series of unipolar pulses with $I_P > I_T$, the trained static configuration between pulses will reflect a highly distorted CDW, with the phase 'stretched' near one end of the sample and 'compressed' near the other end. A sudden reversal of pulse polarity initially results in the CDW unleashing this stored phase, leading to a sudden anomalously large phase velocity transient with a correspondingly small voltage response. Once the stored phase is exhausted, the CDW assumes a steady state velocity limited by damping. The time scale for CDW depolarization is on the order of 5–20 μs in $NbSe_3$ (Gill 1981) and 100–500 μs in $K_{0.3}MoO_3$ (Fleming and Schneemeyer 1983).

A closely related memory effect concerns the phase of the coherent noise oscillations. To observe the effect, the CDW is excited by a steady state current with $I_s > I_T$, and the noise oscillations riding on the voltage response are observed in real time. The current is then suddenly driven to zero at time t' and reinstated at a later time t''. The phase with which the oscillations resume at t'' is found (Gill and Higgs 1983) to be exactly the same as the phase with which the oscillations ceased at t'. Hence, during the zero drive static situation between t' and t'', the CDW is in a metastable state which retains the phase information of the earlier sliding state. Variations in temperature during the static situation erase the phase memory.

Both of the above-mentioned memory effects are closely related to 'pulse

synchronization', a form of Shapiro step interference viewed in the real-time domain. Pulse synchronization was first observed by Fleming (1982). A train of unipolar rectangular current pulses is applied to the sample and the voltage response is observed in real time on an oscilloscope. As the amplitude of the current pulse I_P exceeds I_T, narrow-band noise oscillations are directly observed. For a given $I_P > I_T$, it is found that the noise oscillations can be enhanced by 'synchronizing' their period to the pulse width. This is accomplished by fine tuning either I_P or the pulse width such that an integral number of noise oscillations 'fit' into the length of the pulse. Causality is satisfied since the memory effect during a particular pulse reflects only the width of the previous identical pulses. An example of pulse synchronization in $NbSe_3$ is shown in fig. 4.9.

During a pulse synchronization experiment, the drive field applied to the sample is precisely of the form eq. (4.1), where E_{dc} is interpreted as the time-average drive signal, and $P(t)$ reflects the positive and negative excursions from E_{dc}. Pulse synchronization may thus be identified as the phenomenon of Shapiro step interference viewed in the time domain. The criterion for pulse synchronization is the same as for Shapiro step interference, eq. (4.3).

From figs. 4.2 and 4.3a, it is apparent that the width of the Shapiro step interference peaks can be substantial, which implies significant noise frequency pulling near the step edges. Analogous frequency pulling can be observed in time domain pulse synchronization experiments on $NbSe_3$ and $K_{0.3}MoO_3$. Figure 4.10 shows the real-time response of $K_{0.3}MoO_3$ to rectangular current pulses. In trace (a), the noise oscillations are clearly visible, and an integral number of oscillations occupy the pulse width. As the pulse width is increased, the noise frequency changes (even though the

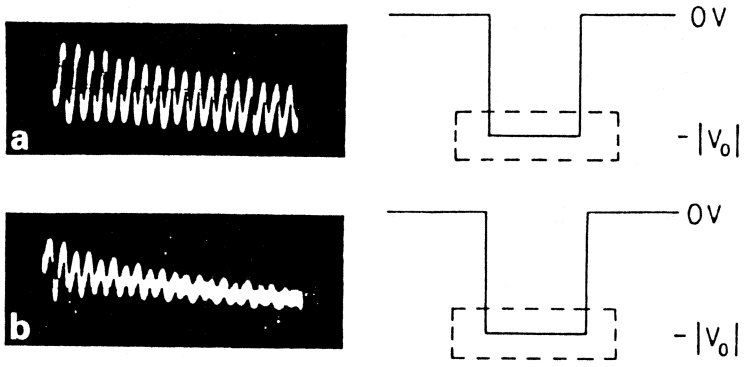

Fig. 4.9. Example of pulse synchronization effect in $NbSe_3$: (a) synchronized; (b) unsynchronized. (From Brown et al. 1986.)

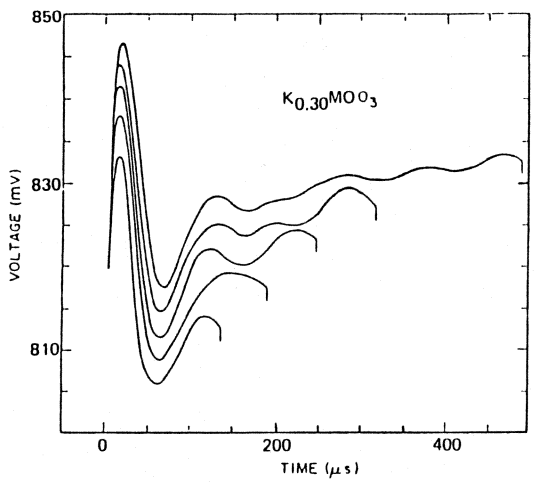

Fig. 4.10. Pulse width memory effect in $K_{0.3}MoO_3$ at 45 K. The pulses have a period of 10 mS; different traces correspond to different pulse widths. (From Fleming et al. 1985.)

height of the current drive pulse remains constant) so that an integral number of oscillations *still* occupies the new pulse width. In other words, changing the ac drive frequency (by changing the drive pulse width) results in a pulling of the noise frequency. Over a substantial range of ω_{ex}, the noise frequency remains locked to a harmonic of ω_{ex}.

In the pulse-induced Shapiro step described in fig. 4.7, saturation of δV occurs for t_1 above approximately 4 μs. This independently identifies a relaxation time comparable to that obtained from pulse memory experiments. The fit of eq. (4.6) to experimental data in fig. 4.7 suggests that a distribution of relaxation times may be more approporiate than a single time scale. The spectrum of times is associated with the development of the pinned state after the high field is turned off. In this sense the behavior is similar to the stretched exponential or logarithmic decay of CDW polarization following a current pulse. However, both the Shapiro step experiments and polarization relaxation experiments probably reflect more a sampling of a large number of metastable states rather than a simple distribution of relaxation times.

A feature of CDW response again related to internal modes, memory, and Shapiro step interference is that of transient ringing, first identified in $NbSe_3$ (Zettl 1983). Ringing refers to the strong decrease in the amplitude of the narrow-band noise oscillations following the start of a current pulse which drives the CDW from below threshold to above threshold. The ringing resembles an inertial effect, not expected in an overdamped system. Ringing only occurs if the CDW is initially started from a static configura-

tion below threshold, and hence does not simply reflect response to a dramatically changing drive (i.e. step function with the associated high harmonic frequency content). The amplitude of the transient after the start of the pulse is also strongly dependent upon the dc bias of the pinned CDW prior to the pulse. This strong sensitivity to initial metastable (pinned) state has been exploited to determine CDW relaxation rates between different

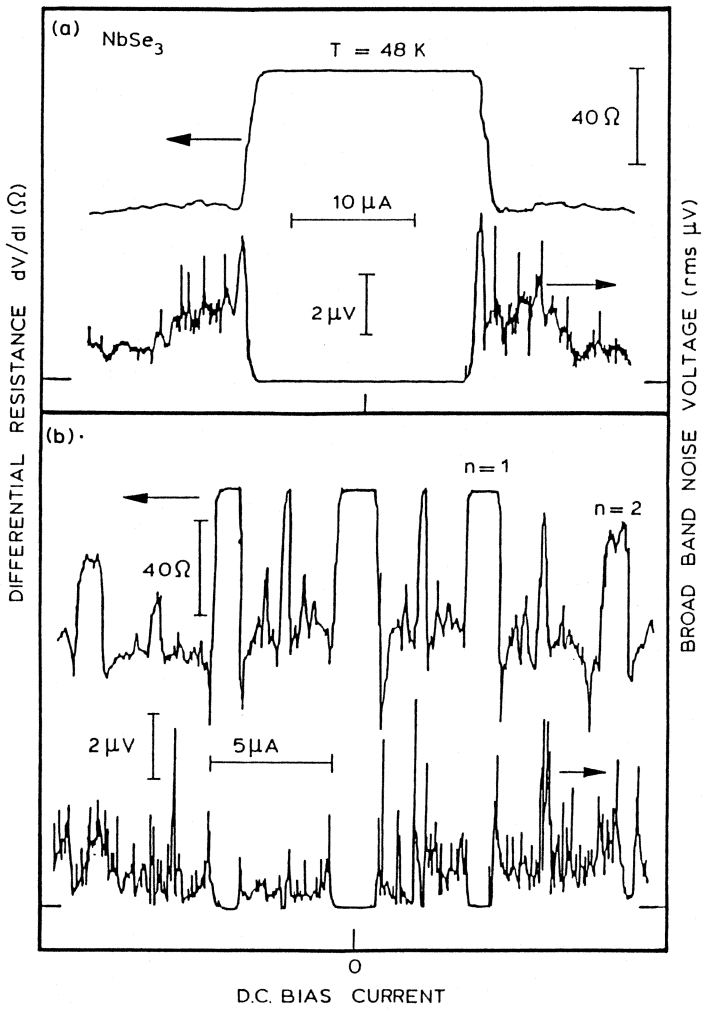

Fig. 4.11. dV/dI and broad-band noise amplitude in $NbSe_3$: (a) no rf, (b) with superposed rf drive. Complete electronic locking is associated with a suppression of broad band noise. (From Sherwin and Zettl 1985.)

metastable pinned states. For $NbSe_3$, it is found (Parilla and Zettl 1985) that relaxation from the metastable state just below threshold to the (polarized) metastable state associated with an unbiased (but trained) CDW takes on the order of 50–100 ns. This relaxation is exceptionally fast and distinct from that associated with the 'waiting time' of Shapiro steps experiments.

It has been suggested that the *broad*-band noise generated by a sliding CDW reflects directly internal CDW degrees of freedom. In the absence of rf radiation, the broad band noise amplitude is a well-defined function of CDW phase velocity. Figure 4.11a shows, for $NbSe_3$, the broad-band noise amplitude as a function of dc bias. In the presence of rf radiation, the CDW phase velocity on a mode locked Shapiro step becomes fixed. Surprisingly, in this locked state the sliding CDW generates no broad band noise (Sherwin and Zettl 1985). This is demonstrated in fig. 4.11b. It has been suggested that during mode locking, the internal degrees of freedom responsible for broad-band noise generation are 'frozen out'. This interpretation suggests that the CDW condensate is exceptionally coherent during mode locking, which has implications for elastic CDW response (see section 7).

4.4. *Many degree of freedom models for the interference*

Single degree of freedom models have not been fully successful in describing Shapiro step interference phenomena. It appears necessary to explicitly treat the CDW as a many degree of freedom system. The hydrodynamical approach of Sneddon, Cross and Fisher (1982) (see section 2.2) predicts (to all orders in perturbation theory) no steady state narrow band noise oscillations. In the presence of ac and dc drive fields, however, interference is obtained. The form of the interference in the $I-V$ characteristics is predicted to be (Sneddon et al. 1982)

$$\mathrm{d}I/\mathrm{d}E \approx v_\mathrm{d}^{-1} J_n^2(gV_\mathrm{ac}/\omega_\mathrm{ex}) G[(gv_\mathrm{d} - n\omega_\mathrm{ex})/v_\mathrm{d}^2], \tag{4.11}$$

where v_d is the dc drift velocity of the condensate, g represents a reciprocal lattice vector, and $G(z)$ is a function peaked at $z = 0$. The model of Sneddon et al. does not predict true mode locking during interference; rather, interference occurs whenever the intrinsic and applied frequencies are relatively close. In addition, the interference features predicted by eq. (4.11) are smooth functions of dc bias, in contrast to the rather sharp Shapiro step interference peaks experimentally observed. Sneddon has extended the classical deformable model to include electrostatic interactions of the CDW with itself (Sneddon 1984), conduction electrons, and the host lattice with defects. The model suggests an important role played by free electron screening. For TaS_3, for example, it is predicted that the wings of the $\mathrm{d}V/\mathrm{d}I$ interference peaks will be strongly enhanced and that

the peak heights will change little as the temperature is lowered in the CDW state. Experimentally, the interference peaks in TaS_3 are observed to broaden with decreasing temperature. Sneddon has further studied (Sneddon 1984) interference effects by extensions of the Frenkel–Kontorova model, where the CDW is treated as interacting discretized units in a periodic potential. The model accounts well for dc field-induced interference structure in the complex ac conductivity of $NbSe_3$ and TaS_3.

Coppersmith and Littlewood (1986) have reexamined the deformable CDW model of Sneddon, Cross and Fisher. The system is discretized and the phase $\phi_i = Qu_i$ at the impurity site becomes

$$\mathrm{d}\phi_i/\mathrm{d}t = [(\phi_{i+1} - \phi_i)/L_i - (\phi_i - \phi_{i-1})/L_{i-1}] + U \sin(\phi_i + \phi_j) + \tfrac{1}{2}E(t)(L_i + L_{i-1}), \tag{4.12}$$

where $\phi_i = QR_i$ is the undistorted phase and $L_i = R_{i+1} - R_i$ is the distance between the impurities. A sinusoidal pinning potential is assumed. In the low-field regime, eq. (4.12) *does* predict true mode locking when ω_{ex} is small and $E_{dc} = E_{ac}$ such that significant relaxation takes place while the drive field is below threshold. Subharmonic mode locking arises from the presence of many pinned metastable states. The experiments of Brown et al. (1986) discussed in section 4.1 (see fig. 4.5) support this model, i.e., it appears that the CDW needs to spend time below threshold for true mode locking to occur. Figure 4.12 shows mode locking predicted by the deformable CDW model with different numbers of random impurities. Both harmonic and subharmonic interference is observed; the appearance of high-order subharmonics is associated with an increase in the number of degrees of freedom. It is interesting to note that, for a drive configuration where the time the CDW is at rest is long compared to the time above threshold ($t_1 \gg t_2$ in fig. 4.6), a single degree of freedom model with *any* potential will yield (even with CDW inertia) *only harmonic* mode locking. This is in contrast to experimental observations, and supports a many degree of freedom model for the Shapiro step interference.

A very large number of degrees of freedom is not necessary to generate subharmonic as well as harmonic mode locking in a classical CDW dynamics model. Matsukawa and Takayama (1987) have considered the case of a set of overdamped coupled oscillators each independently obeying eq. (4.7). Subharmonic interference is obtained for as few as two coupled oscillators. For two linearly coupled oscillators in a sinusoidal potential, the equations of motion are

$$\mathrm{d}\phi_1/\mathrm{d}t = \phi_2 - \phi_1 + \sin\phi_1 + E_{dc} + E_{ac}\cos\omega_{ex}t, \tag{4.13a}$$

$$\mathrm{d}\phi_2/\mathrm{d}t = \phi_1 - \phi_2 + \sin(\phi_2 + \delta) + E_{dc} + E_{ac}\cos\omega_{ex}t. \tag{4.13b}$$

Equation (4.13a,b) predict subharmonic mode locking unless $\delta = 0$. Figure

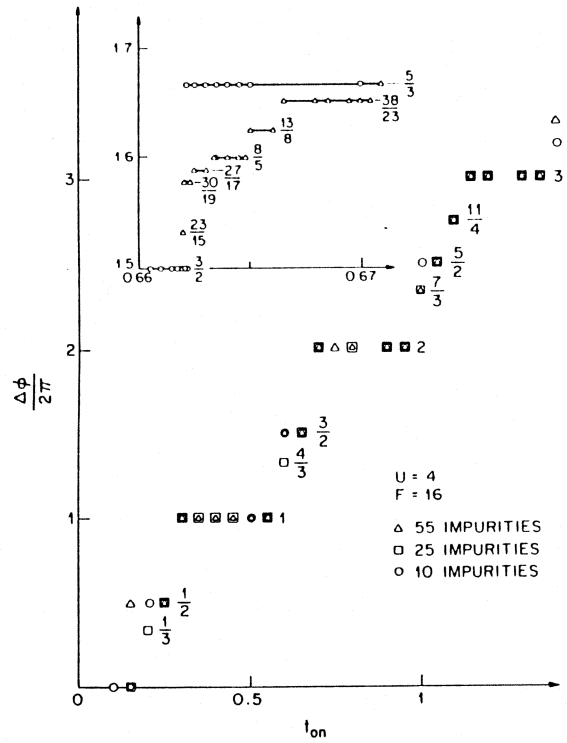

Fig. 4.12. Mode locking in the many-degree-of-freedom model of eq. (4.12). The vertical axis is the number of wavelengths moved per pulse, plotted versus the pulse duration t_{on} with a fixed $E_{on} = 16$ and $U = 4$. Three different numbers of degrees of freedom are shown: 10, 25 or 55. Locking is demonstrated because the number of wavelengths moved is always a rational fraction. Inset: magnified portion of the plot, demonstrating that increasing the number of degrees of freedom causes the appearance of high-order subharmonics (from Coppersmith and Littlewood 1986).

4.13a shows the I–V characteristics of this model with $\delta = \pi/2$. A rich spectrum of mode locking is observed, in good qualitative agreement with experiment. No chaos is predicted, even for large E_{ac}, again consistent with experiments on conventional $NbSe_3$ samples. Figure 4.13b shows mode locking in the E_{ac}–E_{dc} plane predicted by eqs. (4.13a,b). The decrease in δV at large ac drive is similar to that observed experimentally (see fig. 4.8).

Recently, it was suggested that CDW memory and associated interference phenomena may be an example of universal 'phase organization'. Tang et al. (1987) consider a 'soft' system with many effective degrees of freedom (such as the Frenkel–Kontorova model with many balls connected with weak springs). If the system driven by a train of rectangular force pulses, the system can be 'trained' such that, at the end of a driving pulse,

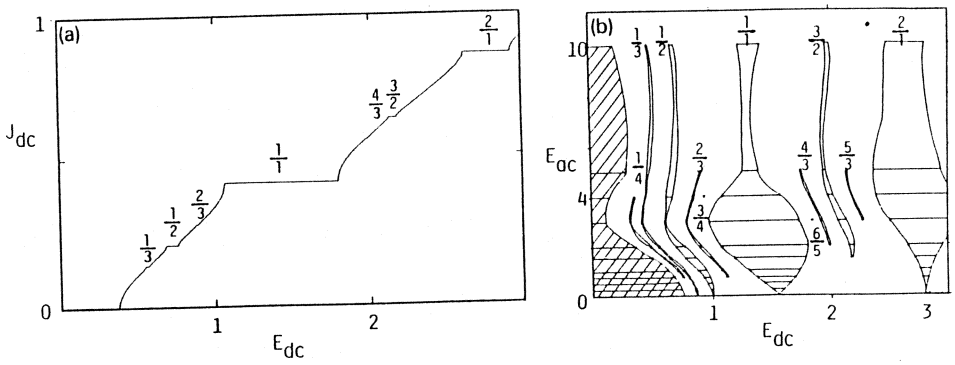

Fig. 4.13. Mode locking for a set of coupled oscillators described by eq. (4.13). (a) Interference in the direct $I-V$ characteristics. The lockings at $q = 1$, 2, and 3 are appreciable. (b) Locking regions in the E_{dc}–E_{ac} plane. (From Matsukawa and Takayama 1987.)

the system will be in a self-organized state. This state can be one that appears *least likely* for the system, e.g., all balls at the tops of the potential peaks! Figure 4.14 shows an example of a phase organized state. The dynamics of the system self-selects certain metastable states; in a CDW experiment, these states may be those most important for strong interference. Hence, universal phase organization provides a natural account of the pulse duration memory effect (fig. 4.10) and associated mode locking in CDW conductors. Central to the phenomenon of phase organization is the presence of many degrees of freedom. This is in contrast to nonlinear dynamics analyses based, for example, on the circle map (see section 5.1), or a small number of coupled oscillators, e.g. eq. (4.13).

Recently, Dong and Yu (1988) have suggested that many 'pseudo-inertial' aspects of CDW dynamics are well described by a single degree of freedom model such as eq. (4.7) with inertia included only for the *sliding* CDW state. Such a description provides good fits to, for example, transient ringing experiments (Parilla and Zettl 1985). On the other hand, the model cannot account well for metastable state structure.

Fig. 4.14. Snapshot of phase organized state of weakly coupled balls in a sinusoidal potential, just prior to the drive field being turned off. (From Tang et al. 1987.)

5. Driven CDWs and the theory of nonlinear dynamics

A driven CDW comprises an exceedingly complex nonlinear system, with many degrees of freedom. The conventional approach in dealing with dynamical systems is to derive a set of differential equations which describes the system, and then integrate the equations to extract the motion. Often, however, the equations of motion are unknown, or, once established, very difficult to solve.

In many systems with a large number of degrees of freedom (such as a fluid), the complex dynamics are actually well described by only a few active degrees of freedom. In such cases it is often advantageous to describe the dynamics in terms of a low-dimensional discrete mapping, rather than by differential equations of motion. A return map relates the state of the system at index $m+1$ (m could be a time unit) to the state of the system at index m. If the points on the mapping fall on a smooth line, the return map is termed one-dimensional. Once the return map for a system has been identified, the evolution of the system can be tracked by simply iterating the map, which in general is far easier than integrating complex equations of motion. Even exceedingly complex system response (such as chaos) is well described by maps. Return maps find a natural application in the description of nonlinear CDW dynamics (Zettl 1988).

5.1. Competing periodicities: the circle map

Interference in CDW systems results directly from the interaction of two competing periodicities, one defined by the narrow-band noise frequency ω_{NBN} and the other defined by the frequency of the external ac drive ω_{ex}. The general phenomenon of competing periodicities has been extensively studied from the point of view of nonlinear dynamics theory (Aizawa and Kobatake 1975, Jensen et al. 1983a,b, 1984, Bohr et al. 1984, Bak et al. 1984).

Consider the quasiperiodic behavior of a system with internal frequency $\omega_{NBN} = d\theta_1/dt$ driven by an incommensurate source at frequency $\omega_{ex} = d\theta_2/dt$. The evolution of the system in phase space can be represented as motion on a two-dimensional torus, as illustrated in fig. 5.1. A particular plane cutting through the torus defines a Poincaré section; in fig. 5.1 the plane has been chosen at $\theta_2 = 0$. The intersection points of the system trajectory with the chosen plane may be obtained by 'strobing' the system at 'times' $\theta_2 = 0$, 2π, 4π, etc., and recording the intersection points in the plane. The series of points thus obtained clearly lie on the intersection of the torus surface with the plane; this intersection is topologically equivalent to a circle. As the system evolves and points accumulate, points on the circle generated during one pass of the system are mapped to another part

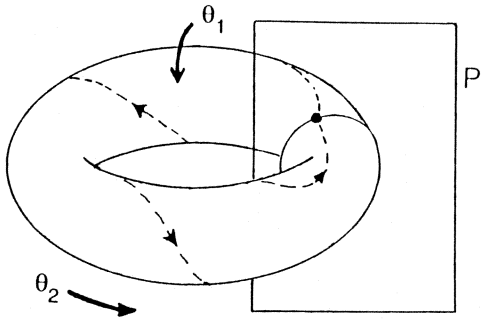

Fig. 5.1. Motion on a 2D torus for a system with two competing periodicities. Phase 1 represents the intrinsic system periodicity; phase 2 represents the external drive periodicity. The dashed line is the trajectory for a $p/q = 3/1$ mode locked state. The Poincaré section contains a single point.

of the circle during the next pass. This defines a nonlinear map of the 'circle onto itself'.

One such mapping of the invariant circle is the sine circle map,

$$\theta_{m+1} = \theta_m + \Omega + (K/2\pi)\sin(2\pi\theta_m), \tag{5.1}$$

a discrete mapping which has been used extensively to describe many natural systems with two competing periodicities (Aizawa and Kobatake 1975, Jensen et al. 1983a,b, 1984, Bohr et al. 1984, Bak et al. 1984). Here $\theta_m = \theta(t = mT)$ with m an integer and $T = 2\pi/\omega_{ex}$. K represents the strength of the coupling between the external drive and the system, and Ω is the ratio of the two characteristic frequencies in the absence of interference (i.e. $\Omega = \omega_{NBN}/\omega_{ex}$). The sine circle map predicts mode locking, subharmonic interference, and a quasiperiodic transition to chaos. Figure 5.2 shows some of the more prominent mode locked regions for the sine circle map in K–Ω space. For $K < 1$, the mode locked steps form an (incomplete) devil's staircase of dimension $d = 1$. Just at $K = 1$, the staircase is complete with a fractal dimension (Jensen et al. 1983a,b, 1984, Bohr et al. 1984, Bak et al. 1984) $d = 0.870$. This is the Hausdorff dimension of the complementary Cantor set for the mode locked region. For $K > 1$, resonances overlap and the map is no longer invertable, hence chaos is possible.

There are two motivations for analyzing CDW interference phenomena in the context of the sine circle map. First, the sine circle map has been found to give a surprisingly accurate account of mode locking in several physical systems with competing periodicities (examples being barium sodium niobate (Martin and Martienssen 1986) and germanium (Gwinn and Westervelt 1987). A second motivation is that detailed numerical and

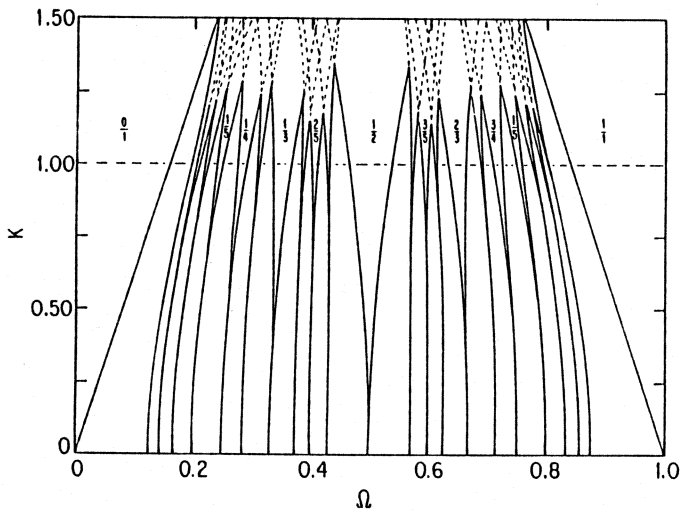

Fig. 5.2. Mode locked regions in the sine circle map. Only a selected set of locked regions is shown. The critical line is at $K = 1$. (From Jensen et al. 1983a,b, 1984, Bohr et al. 1984, Bak et al. 1984.)

analytic calculations (Jensen et al. 1983a,b, 1984, Bohr et al. 1984, Bak et al. 1984) have demonstrated that, for a certain parameter range, the sine circle map is the appropriate return map for the damped pendulum equation, eq. (4.7), which forms the basis of the rigid particle classical model of CDW motion.

The first analysis (Brown et al. 1984) of CDW interference in terms of the circle map addressed the fractal dimension of the locked and unlocked region in a Shapiro steps experiment. To analyze experimental data such as shown in fig. 4.3a, one could count up the widths of all mode locked regions in Ω space, and to test for completeness of the devil's staircase determine if the quasiperiodic orbits (gaps) are confined to a Cantor set of zero measure. A more practical (finite resolution) method is to consider the behavior of the gaps (Brown et al. 1984, Jensen et al. 1983a,b, 1984, Bohr et al. 1984, Bak et al. 1984). Given a scale r, the total measure of the gaps between the mode locked steps is $1 - S(r)$, and the number of holes $N(r) = [1 - S(r)]/r$. If $rN(r) \to 0$ as $r \to 0$, the staircase is complete, with fractal dimension d given by

$$N(r) \propto r^{-d}. \tag{5.2}$$

Such an analysis for $NbSe_3$ by Brown et al. (1984) is shown in fig. 5.3. The data lie on a line whose slope indicates a fractal dimension $d = 0.91$, close to the expected value of 0.87 and hence suggestive that the system is close

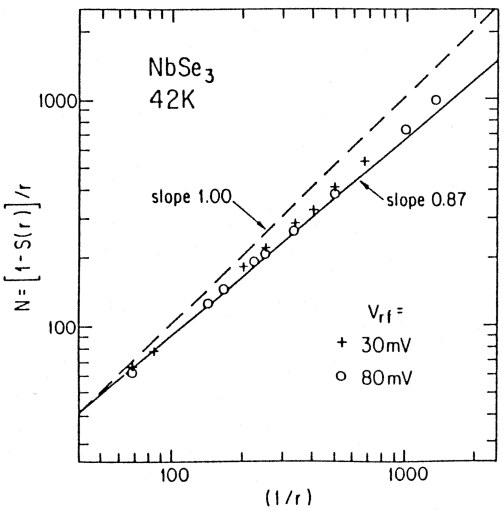

Fig. 5.3. Fractal dimension determination of Shapiro step locking in $NbSe_3$. The data lies close to $d = 0.87$ expected from the circle map at the critical line. (From Brown et al. 1984.)

to criticality and chaotic response. However, no critical line or chaotic response has been identified, even for a large range of ac drive amplitudes. More systematic studies by Sherwin et al. (1988) have also demonstrated that d is strongly ac amplitude dependent in $NbSe_3$, and tends to approach 1 for large ac drive. In the context of the circle map, mode locking in $NbSe_3$ is always subcritical (i.e. $K < 1$).

In comparing the predictions of the sine circle map to CDW response, it seems natural to associate K in eq. (5.1) directly with E_{ac}, and Ω with E_{dc}. A plot of mode locking in the E_{ac}–E_{dc} plane for a CDW system might then be analogous to fig. 5.2 for the circle map. Such direct comparison, however, reveals serious discrepancies, such as the experimentally observed oscillatory behavior of δV with increasing E_{ac} (see figs. 4.4 and 4.8), and the lack of chaotic response at high ac drive. These problems suggest that the driven CDW condensate is not the best physical realization of the sine circle map, at least not if K is directly associated with E_{ac} (in section 5.2.2, it is argued that this direct association is flawed). The physical significance of a well-defined fractal dimension corresponding to the mode locking in $NbSe_3$ is not clear.

5.2. CDW switching and transitions to chaos

For most CDW crystals the CDW condensate depins smoothly as an applied dc bias exceeds threshold E_T; the functional form of the I–V characteristic

is similar to the Zener tunneling expression. However, not all samples of a given material display smooth depinning. In selected crystals of $NbSe_3$, TaS_3, $K_{0.3}MoO_3$, and $(NbSe_4)_{3.33}I$, the CDW depins in a sharp, hysteretic manner which results in a strong discontinuity in the dc $I-V$ characteristics. This phenomenon was first observed in the lower CDW state of $NbSe_3$ by Zettl and Grüner (Zettl and Grüner 1982), and it is referred to as switching.

Switching typically occurs only over a limited temperature range for a given sample. The switching state is characterized by a temperature independent depinning field (Hall and Zettl 1984), $I-V$ hysteresis (Zettl and Grüner 1982), negative differential resistance (Hall et al. 1984), inductive ac response (Hall and Zettl 1985), and large phase polarization (Hall et al. 1988). In the presence of combined ac and dc drive fields, switching samples show unusual Shapiro step structure and period doubling routes to chaos (Hall et al. 1984). Switching can be induced by strong impurity doping or irradiation, and it appears to arise from isolated 'ultrastrong' impurity pinning within the crystal bulk (Hall et al. 1988). The observed velocity discontinuities (Hall et al. 1986) in switching crystals imply local, periodic collapse of the CDW amplitude at phase slip centers. Consequently, one of the most interesting aspects of CDW switching is that to successfully model the phenomenon, it is necessary to include degrees of freedom for *both* the CDW amplitude and phase. This is in contrast to most models of CDW conduction (see section 2) which treat the CDW amplitude as rigid and assign degrees of freedom only to the CDW phase. Switching in $NbSe_3$ has been extensively studied experimentally (Sherwin et al. 1988, Hall and Zettl 1985, Hall et al. 1988) and theoretically (Inui et al. 1988).

5.2.1. Mode locking and chaos

Figure 5.4 shows Shapiro steps interference phenomena in a switching crystal of $NbSe_3$ (Hall et al. 1984). The interference steps in this voltage-driven experiment are the roughly horizontal plateaus whose differential resistance is equal to the low-field pinned state differential resistance. Switching samples show dramatic mode locking. In the trace corresponding to $V_{rf} = 28$ mV in fig. 5.4, for example, complete mode locking, with little space between harmonic mode locked steps, is observed over a large range of dc bias.

On any particular mode locked Shapiro step shown in fig. 5.4, the time averaged dc CDW velocity is constant and insensitive to dc bias. One might expect, on a mode locked step, that higher frequency fluctuations are suppressed, as is the case for non-switching samples (Sherwin and Zettl 1985). For switching samples, however, the situation is quite different; indeed, some of the most complex CDW response occurs precisely when the condensate is mode locked in the dc limit! Figure 5.5a shows an expanded view of mode locked Shapiro steps in switching $NbSe_3$ similar to

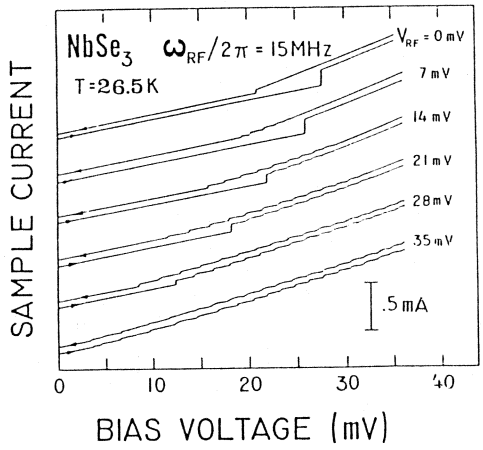

Fig. 5.4. Mode locking in direct I–V traces of switching $NbSe_3$. (From Hall et al. 1984.)

those seen in fig. 5.4. The solid line response is measured at zero frequency. The arrows indicate forward and reverse voltage bias sweep direction, and the traces have been vertically offset for clarity. The CDW is nearly always harmonically mode locked. Figure 5.5b shows the corresponding response spectrum in the frequency domain, for selected dc bias voltages on a particular mode locked step. Complex response is obtained, with an apparent period doubling route to chaos with increasing dc bias. The first frequency spectrum shows only the fundamental of the rf drive at frequency $f = \omega_{ex}/2\pi = 5$ MHz, and higher harmonics of f due to the non-linearity of the CDW system. In the second spectrum, peaks appear at $f/2$, indicating that a period doubling bifurcation has occurred. The third spectrum shows a generally elevated noise level and new frequency structure indicative of a second period doubling bifurcation. The final spectrum shows broad-band chaotic response. The bifurcation points are shown schematically in fig. 5.5a as vertical lines separating different response forms. It is apparent that on each mode locked step, there is a period doubling route to chaos. Such behavior is only observed in switching samples, and thus far it has only been observed in $NbSe_3$ although it probably exists in other switching CDW materials as well.

Figure 5.6a shows the structure of mode locking in the E_{ac}–E_{dc} plane for switching $NbSe_3$ (Sherwin et al. 1988). At the lowest value of ac drive shown (top of fig. 5.6a) there is a hysteretic transition between the $n = p/q = 0/1$ and 1/1 steps, and the $n = 1/2$ step is eclipsed. There is no gap between the 0/1 and 1/1 steps. The period doubling route to chaos is most strongly developed in this region of very hysteretic mode locking. At higher values of ac drive (lower in fig. 5.6a), the $n = 1/2$ step emerges and a

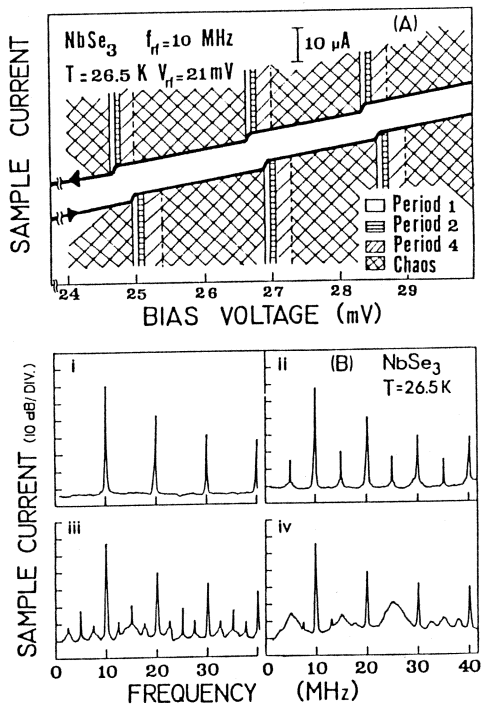

Fig. 5.5. (a) Schematic representation of current response in voltage-driven Shapiro step region of switching $NbSe_3$. The heavy solid lines are the I–V characteristics. A period doubling route to chaos is observed on each mode locked step. Forward and reverse current sweeps have been vertically offset for clarity. (b) Frequency spectrum of current response for selected dc bias. External rf drive frequency and amplitude as in (a). (i) $V_{dc} = 25$ mV, period 1; (ii) $V_{dc} = 25.1$ mV, period 2; (iii) $V_{dc} = 25.2$ mV, period 4; (iv) $V_{dc} = 25.5$ mV, chaos. (From Hall et al. 1984.)

smaller fraction of parameter space is occupied by the mode locked regions. Some period doubling instabilities still exist, but they occur less frequently. Below the critical line identified at $V_{rf}/V_c = 0.97$, period doubling instabilities are no longer observed, and the $n = 1/2$ step shrinks in relative magnitude. In general the response is a very complicated function of ac amplitude and frequency, dc bias, and temperature.

5.2.2. Models for the switching and chaotic response

Mode locking in switching CDWs has many of the characteristics of inertial, underdamped motion. Another way of writing eq. (4.4) in dimensionless form is (Hall et al. 1984, D'Humieres et al. 1982)

$$\beta\, \mathrm{d}^2\varphi/\mathrm{d}t^2 + \mathrm{d}\varphi/\mathrm{d}t + \sin\varphi = e_{dc} + e_{ac}\sin(\Omega_s t), \tag{5.3}$$

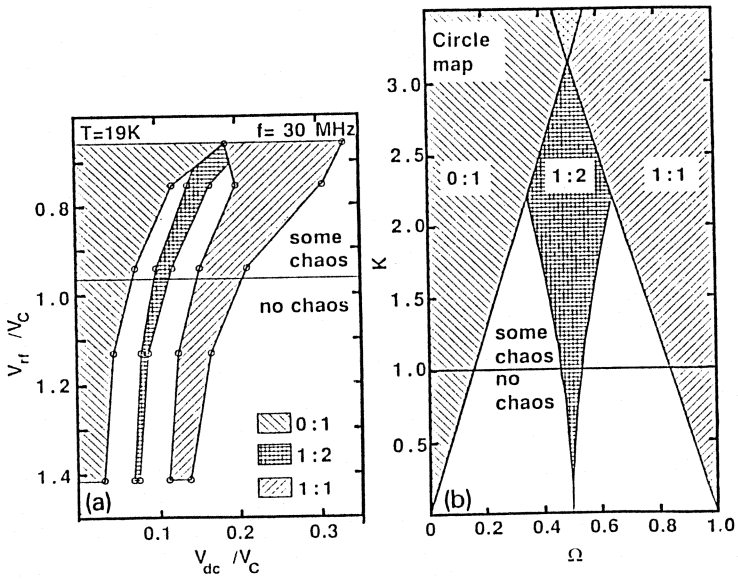

Fig. 5.6. (a) $p/q = 0/1$, 1/2, and 1/1 mode locked regions of switching $NbSe_3$. Period doubling and chaos are observed only above the solid horizontal line at $V_{rf}/V_c = 0.97$. (b) Predictions of the sine circle map. Note the similarity to (a). (From Sherwin et al. 1988).

where β quantifies system inertia, e_{dc} and e_{ac} are dc and ac drive fields normalized to the threshold field E_T, and Ω_s is the ac drive frequency scaled to $\omega_0^2\tau$. In this representation the inertial parameter is more transparent. The solutions of eq. (5.3) with finite β show (D'Humieres et al. 1982, Kautz 1981) many of the features of driven switching CDWs, including hysteresis, mode locking, and chaos. For $\beta > 1$ (underdamped motion), hysteretic Shapiro steps are predicted, and period doubling routes to chaos are observed on some of the mode locked steps (Kautz 1981). However, eq. (5.3) fails to account in detail for switching CDW response. For example, the ac conductivity of a switching CDW with no applied dc field appears overdamped, inconsistent with eq. (5.3) when β is extracted from the switching $I-V$ characteristics. Equation (5.3) also predicts chaotic response for the limited frequency range $\beta^{-1} < \omega_{ex} < \beta^{-1/2}$, inconsistent with experimental observations of chaos in $NbSe_3$ over a much larger frequency range (Hall et al. 1984). Finally, the period doubling route to chaos of eq. (5.3) is not periodic in dc bias, in contrast to the experimental data of fig. 5.4 Thus eq. (5.3) does not provide an entirely satisfactory description of CDW dynamics in either switching or non-switching CDWs.

Recent studies (Sherwin et al. 1988) have re-examined the applicability of the sine circle to CDW dynamics. Although the circle map does not provide

a good description for mode locking in non-switching CDWs, it is surprisingly successful in describing the complex behavior of switching CDWs! Figure 5.6b shows for the sine circle map the mode locked regions $p/q =$ 0/1, 1/2 and 1/1 in K–Ω space. The critical line at $K = 1$ is indicated. For $K < 1$, the circle map predicts distinct mode locked, and quasiperiodic, solutions, but no period doubling or chaos. For $K > 1$, the circle map has a local maximum, with different possible states of the system for a given set of drive parameters. At the edges of the $p/1$ and $p/2$ regions for $K > 1$, the solutions represent simple mode locking. However, as Ω is swept toward the center of the mode locked regions, period doubling instabilities and chaos occur for this range of K. For both the CDW and the circle map, the structure of mode locking and the period doubling route to chaos are periodic in dc bias.

A comparison between figs. 5.6a and 5.6b shows a surprising correspondence between the CDW response and behavior predicted by the circle map. It is interesting that the data indicate that K is *inversely* related to E_{ac}, i.e. large E_{ac} corresponds to small K. This inverse relation reflects a general feature of many nonlinear systems: when forced sufficiently strongly, the nonlinearity of the system becomes a mere perturbation to a linear system. This 'linearizing' effect accounts for the decreasing widths of Shapiro steps with increasing ac drive for both switching and nonswitching CDWs.

The observation of period doubling in mode locked switching CDWs indicates that mode locking in this system can be supercritical, i.e. $K > 1$. The critical line in fig. 5.6a separates regions in which period doubling (not necessarily chaos) is and is not observed experimentally in $NbSe_3$. The dimension of the mode locked regions along this line should be a lower bound to the dimension predicted by the circle map at $K = 1$. Sherwin et al. (1988) have found that $d = 0.85 \pm 0.05$ at the critical line of switching $NbSe_3$, in agreement with the circle map predictions.

The structure of mode locking in switching CDWs is seen to be consistent with the predictions of the circle map in nontrivial ways: (1) The presence of dynamical instabilities is correlated with the width of mode locked steps. (2) The structure of mode locking and the period doubling route to chaos are periodic in dc bias. (3) The period doubling cascade occurs as the system is pushed from the edge of mode locked regions toward the middle of those regions. (4) The fractal dimension of the devil's staircase (Cantor set complementary to the mode locked regions) at the critical line is within experimental error of theoretical predictions.

The success of the circle map in describing the complex response of switching CDWs in the presence of ac and dc drive fields unfortunately gives no insight into the microscopic origins of the unusual dynamics. It has been demonstrated by Hall et al. (1986, 1988) that phase slip processes

within the crystalline bulk are integral to the switching process. Phase slip gives rise to an apparent motion-dependent inertia which can qualitatively account (Inui et al. 1988) for harmonic and subharmonic mode locking, and period doubling routes to chaos. The phase slip process requires a macroscopic polarization of the CDW prior to the collapse of the CDW amplitude. After the amplitude collapses, a finite time is needed for the CDW to depolarize before it can slide. This lag in the response resembles system inertia (response lags the force). When the phase slip process is entrained at a frequency of order the inverse of the relaxation time, the tendency of the CDW to follow the external forcing may compete with the requirement that the CDW 'remember' its previous polarization state (see section 4.3). This competition leads to a frustrated subharmonic or chaotic response.

The detailed dynamics of a CDW condensate with associated phase slip centers has been examined by Hall et al. (1986) and Inui et al. (1988). In simplified form, the equations of motion for the CDW condensate are

$$\mathrm{d}\phi_{\mathrm{bulk}}/\mathrm{d}t = e - \sin\phi_{\mathrm{bulk}} - \alpha\Delta(\phi_{\mathrm{bulk}} - \phi_{\mathrm{psc}}), \tag{5.4a}$$

$$\kappa\,\mathrm{d}\Delta/\mathrm{d}t = -(\Delta + [\phi_{\mathrm{bulk}} - \phi_{\mathrm{psc}}]^2/\Theta^2 - 1), \tag{5.4b}$$

$$\phi_{\mathrm{psc}} \rightarrow \phi_{\mathrm{psc}} \quad \text{if} \quad \Delta > 0, \qquad \phi_{\mathrm{psc}} \rightarrow \phi_{\mathrm{psc}} \pm 2\pi \quad \text{if} \quad \Delta \leqslant 0, \tag{5.4c}$$

where ϕ_{bulk} represents the bulk CDW phase. ϕ_{bulk} couples to a normalized electric field e, an impurity pinning potential $\sin\phi_{\mathrm{bulk}}$, and a strongly pinned phase ϕ_{psc} at the phase slip center. ϕ_{psc} changes by hops of 2π when the CDW amplitude Δ at the strong pinning site collapses, and Δ obeys simple relaxational dynamics driven by the square of the phase polarization, $(\phi_{\mathrm{bulk}} - \phi_{\mathrm{psc}})^2$. α represents the stiffness of the phase mode, κ is the ratio of phase to amplitude relaxation rates; and Θ is the stiffness of the amplitude mode.

Equations (5.4a)–(5.4c) are intractable analytically, but solutions have been obtained by numerical integration on a digital computer (Inui et al. 1988). Figure 5.7 shows the predicted response for a Shapiro step experiment in the E_{ac}–E_{dc} plane. The amplitude relaxation rate has been fixed at $\kappa = 0.5$. Typically, solutions in fig. 5.7 are periodic and mode locked to harmonic (p/q = integer) Shapiro steps. The solutions are identified with the step index n and period P as (n, P). The blank areas in fig. 5.7 represent quasi-periodic or subharmonically mode locked solutions. In typical CDW experiments, the ac field amplitude is held constant and the dc bias is swept through a range of values. The horizontal line in fig. 5.7 corresponds to an analogous sweep. As e_{dc} increases along this line, solutions move through the third harmonic Shapiro step, then through the fourth harmonic Shapiro step, and finally through an unlocked region to the fifth harmonic Shapiro step. Figure 5.8 shows the details of this sweep. The dashed line in the figure represents the entrainment ratio (Shapiro step

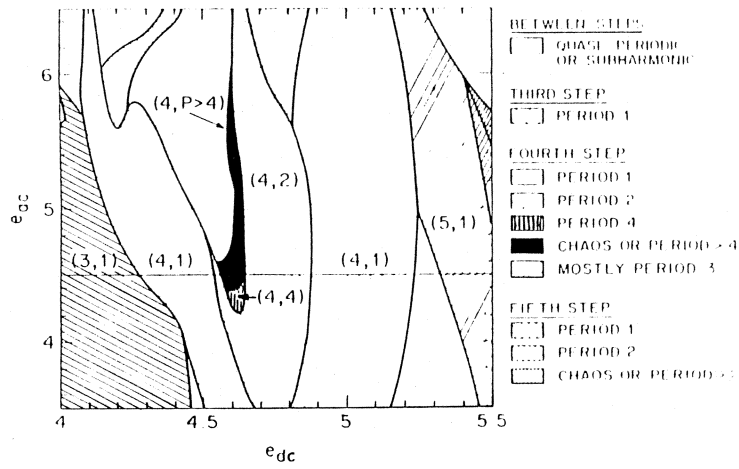

Fig. 5.7. Predicted response of phase-slip model of switching, eqs. (5.4a)–(5.4c). Harmonically mode locked solutions are characterized by an index pair (n, P) which represents their entrainment n and periodicity P. (Boundaries between different regions are approximate). (From Inui et al. 1988.)

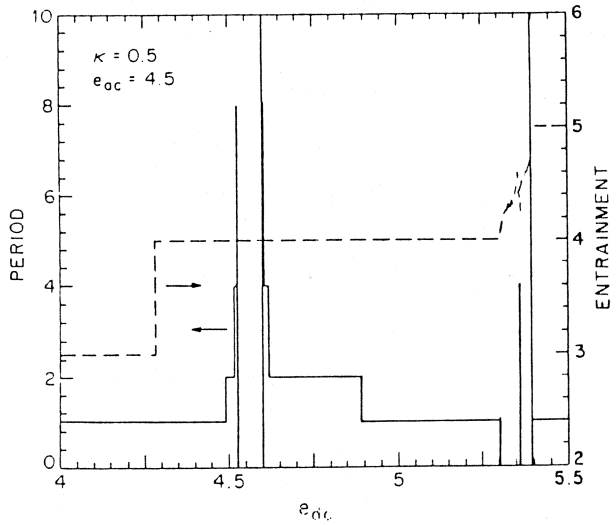

Fig. 5.8. A dc sweep along the solid horizontal line of fig. 5.7. The dashed and solid lines respectively indicate the entrainment and periodicity of solutions found in this range of dc bias. (From Inui et al. 1988.)

order). Over most of the figure, solutions are mode-locked to a *harmonic* step, similar to what is observed experimentally in the switching regime of $NbSe_3$ (figs. 5.4 and 5.5a). For example, the third Shapiro step in fig. 5.8 extends from $e_{dc} = 4.0$ to 4.3; the fourth step from 4.3 to 5.3, and the fifth step from 5.4 to 5.5.

The solid line in fig. 5.8 represents the periodicity index P (quasi-periodic and chaotic solutions are assigned $P = 0$). Even though solutions are usually mode-locked at dc in fig. 5.8, the periodicities of the solutions are often *not* one. For example, on the fourth Shapiro step, a period doubling cascade to chaos is observed. The corresponding response in the frequency domain is shown in fig. 5.9 for selected values of dc bias in this cascade. The behavior on this step is remarkably similar to that observed in $NbSe_3$, as shown in fig. 5.5b. Nearly all of the unusual mode locking and chaotic response features of switching CDWs are, at least qualitatively, well accounted for by the phase slip model of switching.

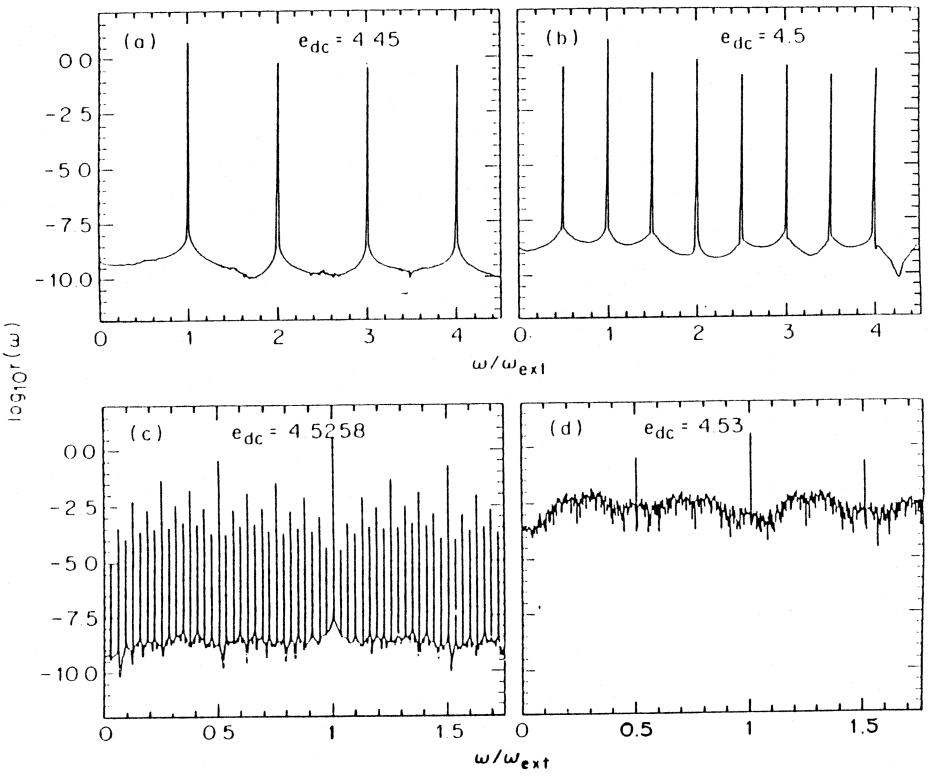

Fig. 5.9. Period doubling route to chaos in the phase slip model of switching induced by increasing dc bias on a particular mode locked step. (From Inui et al. 1988.)

6. Relevant length scales and domain structure

6.1. Intrinsic phase and velocity domains

The static CDW is characterized by a finite static phase coherence length given by the Fukuyama–Lee–Rice length (Lee and Rice 1979)

$$L_s = 2\pi/n_i V_0^2, \tag{6.1}$$

where V_0 is the strength of the impurity potential and n_i is the impurity concentration. L_s is roughly the length over which the phase fluctuations $\langle \delta\phi^2 \rangle^{1/2}$ is less than 2π. For most CDW conductors, L_s is estimated to be on the order of one micron or less, consistent with lower bounds extracted from X-ray scattering measurements. For a dynamic CDW, several new length scales come into play. The dynamic phase–phase correlation length $\langle \phi(0)\phi(x) \rangle$ of a dc-driven sliding CDW condensate has been estimated (Mozurkewich and Grüner 1983) from the narrow-band noise studies, and implies a microscopic domain volume $\Omega_d = 0.2\ \mu m^3$. Within this domain the phase of the CDW behaves more or less as a rigid entity. As the sample volume increases, different microscopic domains oscillate out of phase, and the narrow band noise amplitude falls as $\Omega_d^{-1/2}$, vanishing in the thermodynamic limit. In this interpretation, the noise is a finite-size effect. The recent observation (Hundley and Zettl 1988) of very coherent and large amplitude narrow-band noise response in ultra-thin $K_{0.3}MoO_3$ crystals supports this interpretation.

The time derivative of the CDW phase defines a CDW phase velocity with an associated narrow band noise frequency. Since mode locking experiments reflect interaction between an external rf field and the narrow-band noise frequency, Shapiro step interference is a useful method to investigate CDW phase velocity coherence and its sensitivity to external ac fields. The phase velocity–velocity correlation function

$$\langle (d\phi(0)/dt)(d\phi(x)/dt) \rangle \tag{6.2}$$

defines an ac-sensitive dynamic velocity coherence length ξ_D which may greatly exceed L_s. ξ_D is dependent on the CDW velocity and the amplitude and frequency of externally applied electric fields (Hall et al. 1987).

In a dV/dI Shapiro step mode locking experiment, the height of the interference peak during mode locking will coincide with the pinned differential resistance only if the *entire* CDW condensate takes part in the interference. Such 'complete' locking is, however, not always observed (compare, for example, figs. 4.3a,b and c). The completeness of mode locking can be influenced by changing sample dimensions (Hall et al. 1987). Figure 6.1a shows Shapiro step interference for a relatively long and thick $NbSe_3$ sample. The height of the $n = 1$ step indicates incomplete locking. If

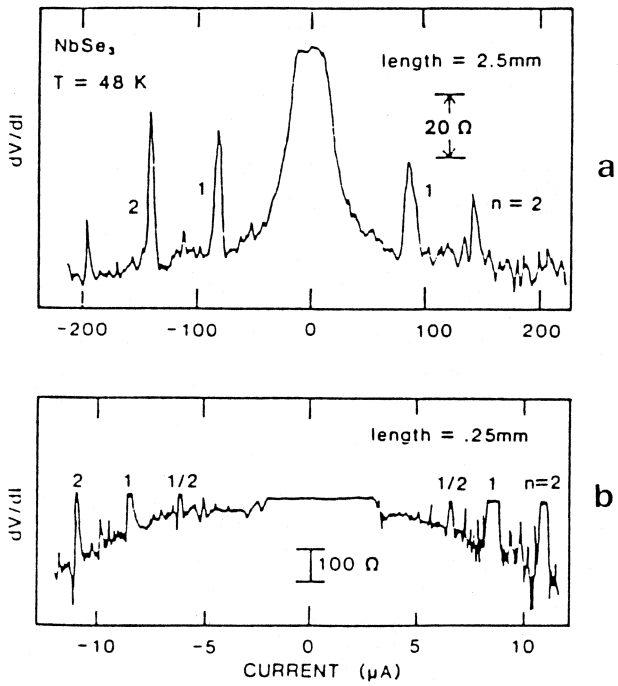

Fig. 6.1. Shapiro step spectrum of $NbSe_3$ crystal. rf frequency is 5 MHz and rf amplitude has been adjusted to maximize the $n = 1$ step height. (a) Original crystal, incomplete locking; (b) Spectrum for a sample cleaved from original crystal. Here sample length and cross-sectional area have both been reduced by a factor of 10. The smaller sample displays complete locking. (From Hall et al. 1987.)

the sample is reduced in volume by decreasing its length and cross sectional area by factors of 10, the interference structure of fig. 6.1b results. Complete locking is now observed. This suggests that large samples are composed of a number of large, macroscopic velocity-coherent domains, which may oscillate at independent frequencies for a given set of drive parameters. The volume of these macroscopic domains may be determined from the Shapiro step interference spectrum.

The height h of the interference peak, measured from the effective base line (or saturated dV/dI value) represents the volume fraction of the CDW condensate mode locked to the external ac drive (Hundley and Zettl 1986, Zettl 1986). This is simply understood if one considers the thin CDW conductor as a linear series of domains. Each domain consists of an independent CDW condensate in parallel with a resistance R_n representing normal electrons. Differences in CDW phase velocity from one domain to the next are compensated for by carrier conversion at domain interfaces.

The CDW associated with each domain has a differential resistance R_{CDW}, where $R_{CDW} \to \infty$ if the domain is mode locked, and $R_{CDW} \to R_c$ (a constant) in the conduction saturated (unlocked) limit. In this model, the total differential resistance for the sample is (Zettl 1986)

$$dV/dI = \sum_{j=1}^{N} R_n R_{CDW}/(R_n + R_{CDW}), \tag{6.3}$$

where j indexes the domain and N is the total number of domains in the crystal. If all N domains are mode locked, $dV/dI = \sum_{j=1}^{N} R_n = dV/dI(I_{dc} = 0)$, and

$$h = h_{max} = \sum_{j=1}^{N} R_n - \sum_{j=1}^{N} R_n R_c/(R_n + R_c).$$

If, on the other hand, only M of the N domains are mode locked,

$$h = \sum_{j=1}^{M} R_n + \sum_{j=M+1}^{N} R_n R_c/(R_n + R_c) - \sum_{j=1}^{N} R_n R_c/(R_n + R_c).$$

This implies that the experimentally determined ratio $h/h_{max} = M/N$, the locked volume fraction.

For a given Shapiro step (indexed by n), the ratio h/h_{max} depends on both the ac electric field amplitude and frequency, and of course the size of the crystal.

To determine $\xi_D(ac)$ explicitly, one may explore mode locking for a single large crystal over different spatial ranges. Figure 6.2 shows the results for such an experiment (Hall et al. 1987) in $NbSe_3$, where non-perturbative 'sliding' voltage sensing probes were used to determine h/h_{max} for the $n = 1$ Shapiro step, as a function of distance d between voltage probes. The

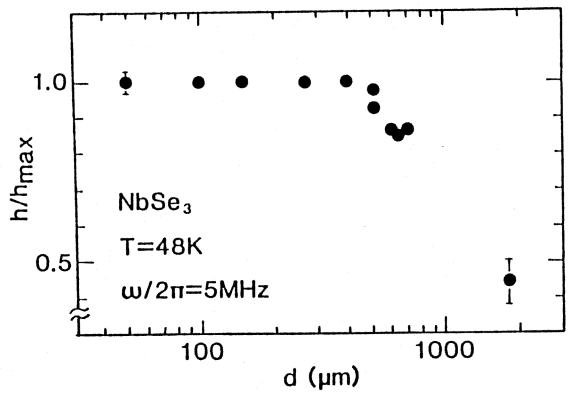

Fig. 6.2. Ratio of h/h_{max} for mode locking in $NbSe_3$ crystal. d is the distance between voltage sensing probes on the crystal surface (from Hall et al. 1987).

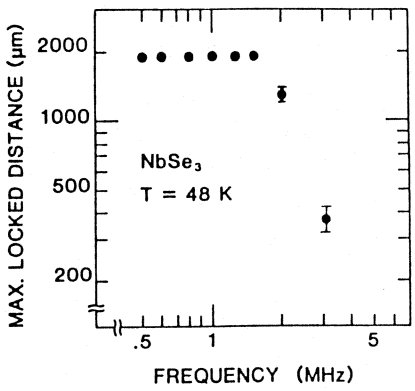

Fig. 6.3. Maximum linear domain size versus rf frequency in $NbSe_3$. For applied frequency less than 2 MHz, the domain size equals the entire sample volume. (From Hall et al. 1987.)

external ac frequency is 5 MHz, and the ac amplitude has been chosen to maximize h/h_{max}. For $d > 500$ μm, h/h_{max} decreases with increasing probe separation, while $h/h_{max} = 1$ for $d < 500$ μm. This determines $\xi_D = 500$ μm for relatively pure specimens of $NbSe_3$. Within a length on the order of 500 μm, all microscopic domains may be fully mode locked by an external ac electric field of frequency 5 MHz.

Using a similar sliding voltage probe method, the frequency dependence of ξ_D has also been explicitly determined (Hall et al. 1987) for $NbSe_3$. For low ω_{ex}, ξ_D may be very large, exceeding the sample length of 0.2 mm in fig. 6.3. Above 2 MHz, ξ_D is seen to drop dramatically with increasing ω_{ex}. Hence at high CDW velocities, the CDW condensate is broken into numerous macroscopic regions with independent phase velocities. Even a very large amplitude rf field is unable to synchronize the regions.

6.2. Temperature gradient effects

An interesting aspect of phase velocity coherence is the effect of an applied uniform temperature gradient. Experiments (Lyding et al. 1986, Ong et al. 1984) have demonstrated that a temperature gradient may split the narrow-band noise spectrum into two or more seemingly independent spectra, with no smearing of the noise peaks. Although such splitting was originally taken as evidence for noise generation at sample contacts (see section 2.5), most experiments point to an interpretation in which the CDW breaks into macroscopic domains, each with a different characteristic phase velocity and oscillation frequency.

The splitting of the noise spectrum in a temperature gradient is reflected also in the Shapiro step spectrum. Figure 6.4 shows the results of such an

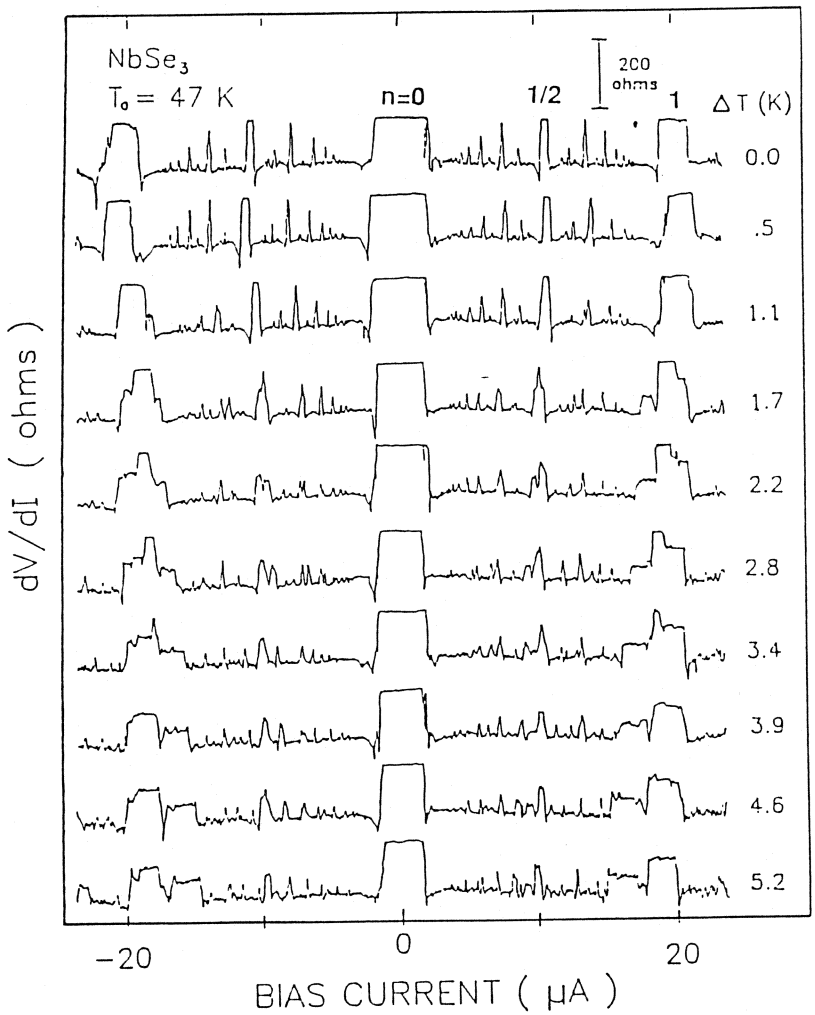

Fig. 6.4. Shapiro step interference in $NbSe_3$ in the presence of an applied temperature gradient. For finite gradient, the sample breaks into independent phase-velocity coherent domains with independent Shapiro step spectra. (From Hundley and Zettl 1986.)

interference experiment (Hundley and Zettl 1986) on $NbSe_3$ performed in the presence of a temperature gradient. Independent interference peaks, associated with mode locking to different macroscopic regions within the sample, are observed. From the ratio h/h_{max} associated with each set of interference peaks, the volumes of the independent regions can be evaluated. The data of fig. 6.4 suggests that the sample has split into two

independent macroscopic domains, with the 'hot' domain comprising 40% of the sample volume and the 'cold' domain comprising 60% of the sample volume. This accounts for 100% of the sample volume. The interface between the macroscopic domains must consist of a phase slip center.

The total number of macroscopic domains within a sample subjected to a temperature gradient represents a competition between the tendency to decrease CDW elastic energy by forming more domains, and the tendency to increase phase slip energy when more domains are formed (with the associated formation of more domain interfaces). A simple model has been proposed by Hundley et al. (unpublished) which explicitly evaluates the balance of elastic and phase slip energy in terms of measurable CDW parameters. Figure 6.5 shows the calculated strain energy, phase slip energy, and total CDW energy as a function of the number of macroscopic domains in a CDW crystal subject to a temperature gradient. The parameters used in the calculation represent those expected for a $NbSe_3$ crystal of length 1 mm and cross-sectional area 5×10^{-7} cm^2, at temperature $T_0 = 48$ K (cold end) with a gradient of 6 K across the sample, and subject to a dc bias current $I_0 = 100\ \mu$A. The total energy is minimized if the sample breaks into three domains, consistent with the number of domains observed in a real $NbSe_3$ crystal under similar experimental conditions (Hundley and Zettl 1986, Lyding et al. 1986).

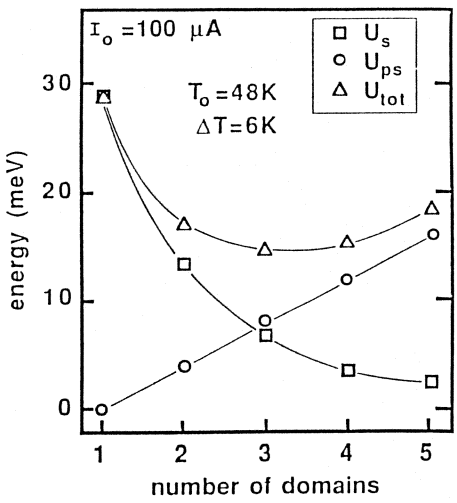

Fig. 6.5. Predicted number of domains for an assumed $NbSe_3$ sample in a temperature gradient. Energy considerations suggest for the indicated set of parameters that the sample should break into three domains (min. energy). (From Hundley et al. unpublished.)

7. Electro-elastic interference

7.1. Elastic mode locking

Electronic mode locking in CDW conductors directly affects the CDW velocity in the interference regime. As discussed in section 4.3, internal degrees of freedom play an important role in the mode locking. Although most attention has been focused on the electronic response of CDW materials, experiments have demonstrated that the *elastic* response of CDW materials is sensitive to CDW motion. Since elastic response involves internal degrees of freedom of the CDW and underlying lattice, it is a useful probe of CDW dynamics, including those of an electronically mode locked condensate.

For most sliding CDW materials (such as $NbSe_3$, TaS_3 and $(TaSe_4)_2I$), the Young's modulus Y and internal friction δ of the crystal change smoothly following CDW depinning (Brill and Roark 1984, Mozurkewich et al. 1985). As first demonstrated by Brill and Roark (1984) for TaS_3, Y decreases with increasing $E_{dc} > E_T$ and eventually saturates; similarly δ increases with increasing $E_{dc} > E_T$ and either saturates or eventually turns over at high field. A simple interpretation of these results is that in the pinned state, the stiffness of the CDW adds to that of the lattice, while a depinned CDW is decoupled from the lattice, and hence the stiffness of the lattice is reduced. Such arguments lead to order of magnitude estimates (Mozurkewich et al. 1985) in changes of Y upon depinning, which are in rough agreement with experiment.

In the region of ac-induced electronic mode locking, where the CDW drift velocity v_d is fixed over a finite range in E_{dc}, one might expect Y and δ to display no more than 'regions of constancy' during mode locking. This would occur if Y and δ were strictly functions of v_d. Alternatively, one might imagine that during mode locking, the CDW would fully decouple from the underlying lattice. In this case, Y and δ would, during electronic mode locking, assume their high field, saturated values.

Figure 7.1 shows that an entirely different behavior is observed (Bourne et al. 1986) for Y and δ during mode locking in TaS_3 and $NbSe_3$. During the Shapiro step interference, Y and δ both tend toward their zero-field, pinned values. This occurs for harmonic as well as subharmonic electronic mode locking. The effect is more dramatic for $NbSe_3$, for which the electronic locking is nearly complete for the $n = 1$ interference step. For both TaS_3 and $NbSe_3$, a rough scaling exists between the degree of electronic mode lock (i.e. h/h_{max}) and the size of the anomaly in Y and δ during mode lock. The anomalies in Y and δ during electronic interference reflect 'elastic mode locking', since here the velocity of sound is locked to a value dictated only by $(d/dt)[\langle d\phi/dt\rangle]$, assuming complete electronic mode locking.

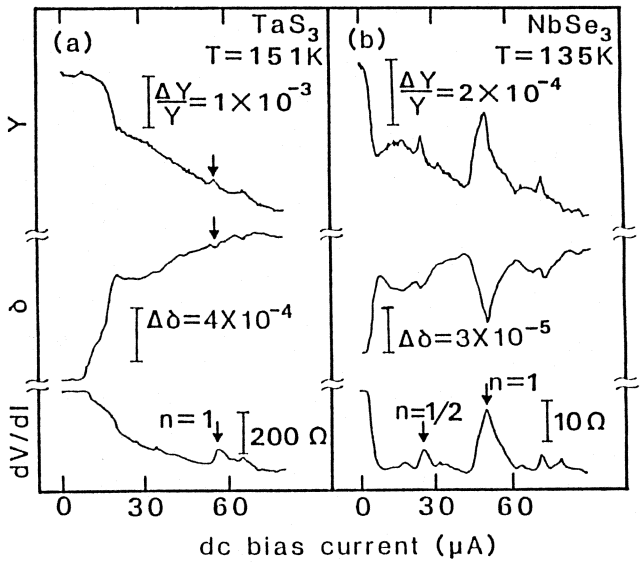

Fig. 7.1. Young's modulus, internal friction, and differential resistance for TaS_3 and $NbSe_3$ in presence of ac + dc electric field drive. Electronic Shapiro step interference is reflected in the elastic constants. (From Bourne et al. 1986.)

7.2. Models for the elastic mode locking

The theoretical models of CDW transport discussed in sections 2 and 4 in general consider only the electronic response, and assume a fully rigid CDW pinning potential. Hence these models fail to account for any elastic properties of the crystal.

Sherwin and Zettl (1986) have attempted to account for elastic mode locking in CDW conductors by an extension of the Frenkel–Kontorova model. The theory treats the CDW condensate and underlying lattice as coupled elastic media obeying classical mechanics. Elasticity of the underlying lattice is incorporated by a discretization which breaks the lattice and associated pinning potential into rigid units of mass M coupled harmonically by springs with spring constant K. The CDW is represented by discrete particles of mass m coupled harmonically to nearest neighbors by spring constant k. Both commensurate and incommensurate CDW cases can be described, and the model is easily extended to the random pinning case. Figure 7.2a shows a mechanical analog representation of the model. The particles in the potential wells are charged CDW 'particles'. Equations of

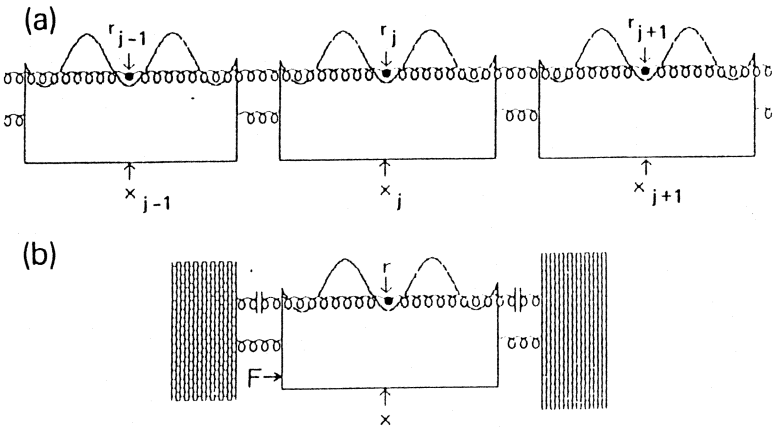

Fig. 7.2. Mechanical analog of electro-elastic coupling model of Sherwin and Zettl: (a) analog of eq. (7.1); (b) analog of eq. (7.2). (From Sherwin and Zettl 1986.)

motion for the model are

$$m\,\mathrm{d}^2 r_j/\mathrm{d}t^2 + \gamma\,\mathrm{d}(r_j - x_j)/\mathrm{d}t + k(2r_j - r_{j+1} - r_{j-1}) + QV\sin[Q(r_j - x_j)] = f_j(t), \quad (7.1a)$$

$$M\,\mathrm{d}^2 x_j/\mathrm{d}t^2 + \Gamma\,\mathrm{d}(2x_j - x_{j-1} - x_{j+1})/\mathrm{d}t + \gamma\,\mathrm{d}(x_j - r_j)/\mathrm{d}t + K(2x_j - x_{j-1} - x_{j+1}) + QV\sin[Q(x_j - r_j)] = F_j(t), \quad (7.1b)$$

where r_j and x_j are respectively the (laboratory frame) positions of the jth CDW mass and jth lattice unit, V is the strength of the impurity pinning potential, and $Q = 2\pi/\lambda$, with λ the CDW wavelength. Γ is the internal friction of the lattice and γ is a frictional coupling between the CDW and lattice. $f_j(t)$ is the force applied to the jth CDW particle by external electric fields, and $F_j(t)$ is the external mechanical force applied to the jth lattice unit. In the limit $K \to \infty$, eqs. (7.1a) and (7.1b) reduce to the discretized Sine–Gordon equation.

A great simplification occurs if the infinite set of CDW particles and lattice units is truncated to three units. This retains the essential physics by preserving internal degrees of freedom and CDW–lattice interactions. With clamped–clamped boundary conditions (appropriate to experimental conditions), the model is reduced to a single renormalized CDW particle interacting with a single renormalized lattice unit. The mechanical analog to the renormalized system is shown in fig. 7.2b. The corresponding equations of motion are (Bourne et al. 1986, Sherwin and Zettl 1986)

$$m^*\mathrm{d}^2r/\mathrm{d}t^2 + \gamma_c\,\mathrm{d}(r-x)/\mathrm{d}t + k_c r + eE_T \sin[2k_F(r-x)] = e[E_{dc} + E_{ac}\cos(\omega_{ex}t)], \quad (7.2a)$$

$$M\,\mathrm{d}^2x/\mathrm{d}t^2 + \Gamma_L\,\mathrm{d}x/\mathrm{d}t + \gamma_c\,\mathrm{d}(r-x)/\mathrm{d}t + K_L x + eE_T \sin[2k_F(x-r)] = F\cos(\omega_r t), \quad (7.2b)$$

where r and x are, respectively, the laboratory positions of the CDW center of mass and lattice, m^* is the total CDW effective mass in the crystal, e the total charge of the CDW, M_L the lattice mass, γ_c and Γ_L respectively the total CDW damping and internal lattice friction, and k_F the Fermi wavevector. k_c and K_L parameterize, respectively, the total elasticity of the CDW and underlying lattice, and $F\cos(\omega_r t)$ is the mechanical force applied to the lattice, the response to which determines the elastic properties of the system. In order for the CDW to slide continuously through the lattice while retaining the periodicity of the pinning potential, k_c is restricted to respond only to ac excitations.

Equations (7.2a,b) have been solved for in the regime of electronic Shapiro step mode locking by an analog computer using parameters appropriate to $NbSe_3$ or TaS_3. Figure 7.3 shows the predicted Y, δ, and $\mathrm{d}V/\mathrm{d}I$ curves as functions of dc bias. Complete Shapiro step mode locking is obtained, with corresponding elastic mode locking in striking agreement with the behavior observed in fig. 7.1. Hence, the mode locking of the elastic response follows directly from a simple model where CDW internal degrees of freedom are taken into account. A model similar to eqs. (7.1a,b)

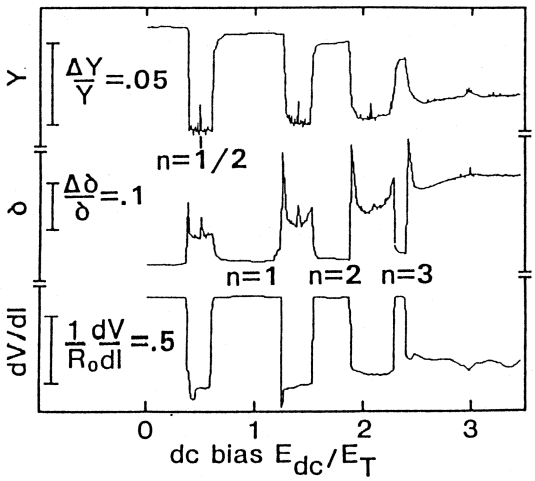

Fig. 7.3. Elastic and electronic response predictions of eq. (7.2) during mode locking. The results agree qualitatively with those observed experimentally in TaS_3 and $NbSe_3$ (fig. 7.1). (From Sherwin and Zettl 1986.)

has been independently proposed by Sneddon (1986), but solved only in the limit of finite E_{dc}, with $E_{ac} = 0$.

8. Conclusion

The intrinsic current oscillations and related ac–dc interference effects in sliding CDW conductors remain among the most fascinating aspects of CDW dynamics. The study of these phenomena is a valuable tool in gaining an understanding of the CDW state. Most experimental evidence points to the narrow band noise oscillations as originating in the bulk. However, phase slip processes cannot be neglected, in particular when they occur at strong pinning sites and lead to switching and related chaotic response, etc. CDW mode locking is one of the most dramatic consequences of CDW nonlinearity and metastability, with many applications to the universal study of competing periodicities and phase organization.

Some of the classical models presented in this review have been surprisingly successful in accounting for very complex CDW response. Models which explicitly take CDW internal degrees of freedom into account are more realistic. The CDW cannot in general be treated as a rigid object in a periodic potential, since in this treatment metastability is lost. Elasticity measurements demonstrate a strong coupling between the CDW electronic response and the underlying phonon structure of the host lattice.

Despite much apparent success of classical models of CDW transport, controversy remains about the applicability of classical concepts to the CDW condensate. Bardeen (unpublished) has strongly criticised all classical approaches to CDW dynamics, and suggests that it is absolutely necessary to treat CDW metals as macroscopic quantum systems with quantum tunneling as an essential feature. Classical concepts are demonstrated to be useful only in the low-frequency response of the pinned CDW or for phenomena on large length scales in the sliding CDW state. Although this criterion puts many CDW interference phenomena into the classical regime, it is expected that, for certain parameter ranges, CDW interference reflects quantum effects. In Bardeen's view, the CDW is not 'like an elastic rug sliding down a staircase with stick-slip friction', but is rather 'a beautiful example of macroscopic quantum mechanics (with many analogies to superconductivity)' (Bardeen unpublished). In either case, CDW dynamics is a unique conduction mechanism with an exceptionally rich spectrum of exotic structural, transport, and mechanical properties.

Acknowledgements

S.B. thanks G. Grüner, L. Mihaly, and G. Mozurkewich for guidance and assistance with experimental measurements, and J. Bardeen, S. Coppers-

mith, P. Littlewood, and R. Thorne for useful discussions. The support of a Postdoctoral Fellowship at Los Alamos National Laboratory is gratefully acknowledged. A.Z. has benefitted from interactions with P. Bak, L.C. Bourne, J.W. Brill, S. Coppersmith, R.P. Hall, M.F. Hundley, M. Jensen, P. Littlewood, P. Parilla, and M.S. Sherwin, and received support from NSF Grant DMR84-00041 and the Alfred P. Sloan Foundation.

References

Aizawa, Y., and Y. Kobatake, 1975, Prog. Theor. Phys. **53**, 305; A.T. Winfree, 1967, J. Theor. Biol. **16**, 15.
Bak, P., T. Bohr and M.H. Jensen, 1984, in: Proc. 54th Nobel Symp. "The Physics of Chaos and Related Phenomena", Graftaavallen, Sweden.
Bardeen, J., Phys. Rev. B (submitted).
Bardeen, J., 1985, Phys. Rev. Lett. **55**, 1010.
Barnes, S.E., and A. Zawadowski, 1983, Phys. Rev. Lett. **51**, 1003.
Bohr, T., P. Bak and M.H. Jensen, 1984b, Phys. Rev. A **30**, 1970.
Bourne, L.C., and A. Zettl, 1987, Phys. Rev. B **36**, 2626.
Bourne, L.C., M.S. Sherwin and A. Zettl, 1986, Phys. Rev. Lett. **56**, 1963; L.C. Bourne and A. Zettl, 1987, Phys. Rev. B **36**, 2626.
Brill, J.W., and W. Roark, 1984, Phys. Rev. Lett. **53**, 846.
Brown, S.E., and G. Grüner, 1985, Phys. Rev. B **31**, 8302.
Brown, S.E., and L. Mihaly, 1985, Phys. Rev. Lett. **55**, 742.
Brown, S.E., G. Mozurkewich and G. Grüner, 1984, Phys. Rev. Lett. **52**, 2277.
Brown, S.E., G. Mozurkewich and G. Grüner, 1985a, Solid State Commun. **54**, 23.
Brown, S.E., G. Mozurkewich and G. Grüner, 1985b, in: Charge Density Waves in Solids, Lecture Notes in Physics, Vol. 217, eds Gy. Hutiray and J. Sólyom (Springer, Berlin) p. 318.
Brown, S.E., G. Grüner and L. Mihaly, 1986, Solid State Commun. **57**, 165.
Cava, R.J., R.M. Fleming, P.B. Littlewood, E.A. Rietman, L.F. Schneemeyer and R.G. Dunn, 1984, Phys. Rev. B **30**, 3228.
Coppersmith, S.N., and P.B. Littlewood, 1986, Phys. Rev. Lett. **57**, 1927.
D'Humieres, D., M.R. Beasley, B.A. Huberman and A. Libchaber, 1982, Phys. Rev. A **26**, 3483.
Dong, J., and L. Yu, 1988, Phys. Rev. B **37**, 6667.
Fack, H., and V. Kose, 1971, J. Appl. Phys. **42**, 320.
Fiory, A.T., 1971, Phys. Rev. Lett. **27**, 501.
Fiory, A.T., 1973a, Phys. Rev. B **8**, 5039.
Fiory, A.T., 1973b, Phys. rev. B **7**, 1881.
Fisher, D.S., 1985, Phys. Rev. B **31**, 1396.
Fleming, R.M., 1982, Solid State Commun. **43**, 167.
Fleming, R.M., and C.C. Grimes, 1979, Phys. Rev. Lett. **42**, 1423.
Fleming, R.M., and L.F. Schneemeyer, 1983, Phys. Rev. B **28**, 6996.
Fleming, R.M., D.E. Moncton and D.B. McWhan, 1978, Phys. Rev. B **18**, 5560.
Fleming, R.M., L.F. Schneemeyer and R.J. Cava, 1985, Phys. Rev. B **33**, 2930.
Fröhlich, H., 1954, Proc. R. Soc. London Ser. A **223**, 296.
Gill, J.C., 1981, Solid State Commun. **39**, 1203.
Gill, J.C., and A.W. Higgs, 1983, Solid State Commun. **48**, 709.
Gor'kov, L.P., 1983, JETP Lett. **38**, 87.

Grüner, G., and A. Zettl, 1985, Phys. Rep. **119**, 117.
Grüner, G., A. Zawadowski and P.M. Chaikin, 1981, Phys. Rev. Lett. **46**, 511.
Gwinn, E.G., and R.M. Westervelt, 1987, Phys. Rev. Lett. **59**, 157.
Hall, R.P., and A. Zettl, 1984a, Phys. Rev. B **30**, 2279.
Hall, R.P., and A. Zettl, 1984b, Solid State Commun. **50**, 813.
Hall, R.P., and A. Zettl, 1985, Solid State Commun. **55**, 307; R.P. Hall and A. Zettl, Phys. Rev. B (in press).
Hall, R.P., M.S. Sherwin and A. Zettl, 1984a, Phys. Rev. Lett. **52**, 2293.
Hall, R.P., M.S. Sherwin and A. Zettl, 1984b, Phys. Rev. B **29**, 7076.
Hall, R.P., M.F. Hundley and A. Zettl, 1986a, Phys. Rev. Lett. **56**, 2399.
Hall, R.P., M.F. Hundley and A. Zettl, 1986b, Physica B **143**, 152.
Hall, R.P., M.F. Hundley and A. Zettl, 1987, Synth. Met. **19**, 813.
Hall, R.P., M.F. Hundley and A. Zettl, 1988, Phys. Rev. B **38**, 13002.
Held, G.A., 1985, Ph.D. Thesis (Univ. of California) [Lawrence Berkeley Laboratory Report No. LBL-20626].
Hundley, M.F., and A. Zettl, (unpublished).
Hundley, M.F., and A. Zettl, 1986, Phys. Rev. B **33**, 2883.
Hundley, M.F., and A. Zettl, 1988, Solid State Commun. (in press); also unpublished work.
Hundley, M.F., P. Parilla and A. Zettl, (unpublished).
Hundley, M.F., W.N. Craeger and A. Zettl, 1988, Bull. Am. Phys. Soc. **33**, 425.
Inui, M., R.P. Hall, S. Doniach and A. Zettl, 1988, Phys. Rev. B **38**, 13047.
Janossy, A., G. Mihaly and L. Mihaly, 1985, in: Charge Density Waves in Solids, Lecture Notes in Physics, Vol. 217, eds Gy. Hutiray and J. Sólyom (Springer, Berlin) p. 412.
Jensen, M.H., P. Bak and T. Bohr, 1983a, Phys. Rev. Lett. **50**, 1637.
Jensen, M.H., T. Bohr, P.V. Christiansen and P. Bak, 1983b, Brookhaven National Laboratory Report No. 33495.
Jensen, M.H., P. Bak and T. Bohr, 1984, Phys. Rev. A **30**, 1960.
Jing, T.W., and N.P. Ong, 1986, Phys. Rev. B **33**, 5841.
Kautz, R.L., 1981, J. Appl. Phys. **52**, 6241.
Lee, P.A., and T.M. Rice, 1979, Phys. Rev. B **19**, 3970; H. Fukuyama and P.A. Lee, 1978, Phys. Rev. B **17**, 535.
Lindelof, P., 1981, Rep. Prog. Phys. **44**, 949.
Link, G.L., and G. Mozurkewich, 1988, Solid State Commun. **65**, 15.
Lyding, J.W., J.S. Hubacek, G. Gammie and R.E. Thorne, 1986, Phys. Rev. B **33**, 4341.
Martin, S., and W. Martienssen, 1986, Phys. Rev. Lett. **56**, 1522.
Matsukawa, H., and H. Takayama, 1984, Solid State Commun. **50**, 283.
Matsukawa, H., and H. Takayama, 1987, Synth. Met. **19**, 7.
Mihaly, L., (private communication).
Monceau, P., J. Richard and M. Renard, 1980, Phys. Rev. Lett. **45**, 43.
Monceau, P., J. Richard and M. Renard, 1982, Phys. Rev. B **25**, 931.
Monceau, P., M. Renard, J. Richard, M.C. Saint-Lager, H. Salva and Z.Z. Wang, 1983, Phys. Rev. B **28**, 1646.
Mozurkewich, G., and G. Grüner, 1983, Phys. Rev. Lett. **51**, 2206.
Mozurkewich, G., P.M. Chaikin, W.G. Clark and G. Grüner, 1985, in the volume of ref. 46, p. 353; Solid State Commun. **56**, 421.
Ong, N.P., and G. Verma, 1983, Phys. Rev. B **27**, 4495.
Ong, N.P., G. Verma and K. Maki, 1984, Phys. Rev. Lett. **52**, 663.
Parilla, P., and A. Zettl, 1985, Phys. Rev. B **32**, 8427.
Shapiro, S.M., 1963, Phys. Rev. Lett. **11**, 80.
Sherwin, M.S., and A. Zettl, 1985, Phys. Rev. B **32**, 5536.
Sherwin, M.S., and A. Zettl, 1986, Physica D **23**, 62.

Sherwin, M.S., A. Zettl and R.P. Hall, 1988, Phys. Rev. B **38**, 13028; see also ref. 77.
Sneddon, L., 1984a, Phys. Rev. B **29**, 719 and 725.
Sneddon, L., 1984b, Phys. Rev. Lett. **52**, 65.
Sneddon, L., 1986, Phys. Rev. Lett. **56**, 1194.
Sneddon, L., M.C. Cross and D.S. Fisher, 1982, Phys. Rev. Lett. **49**, 292.
Tang, C., K. Wiesenfeld, P. Bak, S.N. Coppersmith and P.B. Littlewood, 1987, Phys. Rev. Lett. **58**, 1161.
Thorne, R.E., W.G. Lyons, J.W. Lyding, J.R. Tucker, J. Bardeen, S.E. Brown and G. Grüner, 1986, Phys. Rev. B **33**, 7342.
Thorne, R.E., W.G. Lyons, J.W. Lyding, J.R. Tucker and J. Bardeen, 1987, Phys. Rev. B **35**, 6360.
Tutto, I., and A. Zawadowski, 1985, Phys. Rev. B **32**, 2449.
Wang, Z.Z., H. Salva, P. Monceau, M. Renard, C. Roucau, R. Ayroles, F. Levy, L. Guemas and A. Meerschaut, 1983, J. Phys. (France) Lett. **44**, L-311.
Zettl, A., 1983, in: Proc. Int. Symp. on Nonlinear Transport and Related Phenomena in Inorganic Quasi-One-Dimensional Conductors, Sapporo, Japan, p. 41.
Zettl, A., 1986, Physica D **23**, 155.
Zettl, A., 1988, in: Methods and Applications in Nonlinear Dynamics, ACIF Series, Vol. 7, ed. A. Saenz (World Scientific, Singapore) p. 203.
Zettl, A., and G. Grüner, 1982, Phys. Rev. B **26**, 2298.
Zettl, A., and G. Grüner, 1983, Solid State Commun. **46**, 501.
Zettl, A., and G. Grüner, 1984, Phys. Rev. B **29**, 755.